A SIMULATION BY USING COHESIVE ZONE MODEL FOR INDENTATION TEST IN THIN-FILM/SUBSTRATE SYSTEMS

YIN YOU SHENG

(B.Sci. Fudan University)

A THESIS SUBMITTED FOR THE DEGREE OF MASTER OF ENGINEERING

DEPARTMENT OF MECHANICAL ENGINEERING

NATIONAL UNIVERSITY OF SINGAPORE

2007

ACKNOWLEDGEMENTS

The author of this master thesis would like to express his sincere appreciation to his supervisor, Dr. Zeng Kaiyang, who has given the author much patient guidance and invaluable advice during the course of this project. This master thesis may not come out in time without Dr. Zeng's encouragement and valuable suggestions. The analysis methodology for scientific research he taught is an important experience for the author.

The author also wants to express his gratitude to Mr. Yeap Kong Boon for both his valuable theoretic advice and adequate experiment data, and these really help the author significantly when performing finite element simulation in this project.

Last but not least, the author wants to thanks to all his family members, who have given him so much support during his growth, and it is very lucky for him to have them.

TABLE OF CONTENTS

SUMMARY

This master thesis presents finite element simulation of interface adhesion properties and interfacial delamination cracking processes of thin film systems during indentation experiments using wedge-shape indenters. The cohesive zone model based on traction separation law (T-S) is employed during the FEM simulation. The cohesive zone model used in this thesis contains three important parameters: interface strength, interface energy and the shape of the traction separation law. This thesis studied the effect of interface strength and interface energy on the initiation of interface delamination and effect of the thickness and properties of the film on the interface adhesion and delamination processes. This thesis also compared the FEM simulation results with the nanoindentation experimental results obtained using two wedge indenters having 90^o and 120^o inclusion angles on thin-film/substrate systems. The similarity and differences between the simulation and experiments are made. Commercial software ABAQUS (version 6.5) is used in this simulation work.

LIST OF FIGURES

LIST OF TABLES

Chapter 1 Introduction

1.1 Background and Objectives

Thin film/substrate systems are found in many important engineering applications such as micro-electronics, optoelectronics, display panels and many other devices. Many techniques, for instance, sputtering, vapor deposition, ion implantation and laser glazing are employed to fabricate thin film/substrate systems.

In the applications mentioned above, one of the most important issue is the properties of interface between film and substrate. Since the delaminations caused by a crack at the interface will lead to the failure of the devices containing the thin film/substrate system, it is therefore very important to study the mechanisms of delamination initiation, and its evolution as well as how to improve the stability and reliability of the interface in the thin film/substrate systems. Interface adhesion is one of the important properties which characterizes the stability and reliability of the interface.

Many experimental techniques have been developed to determine the interface adhesion properties. Nanoindentation is one of the methods used for this purpose. Nanoindentation technique has been used as a convenient and most straight forward method to measure the mechanical properties of thin film/substrate systems for dozens of years. This method is also used to characterize the interface adhesion properties. However, because of the

difficulties in interpreting experimental data, there are still many challenging issues to be understood in order to make this method more useful to characterize the interface properties.

This thesis therefore used a finite element method (FEM) with cohesive zone model to simulate the nanoindentation experiments and to study the mechanical characteristics of the thin film/substrate interfaces with (1) different material properties of thin films and substrate; (2) the different inclusion angles of the indenter tips. It is assumed that there is a cohesive zone ahead of the crack tip at the interface, which consists of upper and lower surfaces held by the cohesive traction. The cohesive traction of the interface is related to the separation displacement between the upper and lower surfaces. The relationship of cohesive traction and the separation displacement is often called as “Traction-Separation law” (T-S law).

During the nanoindentation experiments, the relationship between the applied load and the penetration depth of the indenter tip into the surface of the materials is recorded and such a curve is usually called the load-displacement curve. The FEM simulation performed in this work has reported this load-displacement curve and the interface delamination initiation is associated with the characteristics of this curve. Further more, these characteristics in the load-displacement curves are discussed when comparing the simulation and the nanoindentation experimental results. From the load-displacement curve, one can find a critical indentation load and a critical

indentation depth associated with the initial delamination crack at the thin film/substrate interface, and using the mechanical analysis, the general properties of interface adhesion can be determined. However, to determine the exact value of interface strength, interface energy and the shape of traction separation law from the indentation load-penetration curve is very difficult due to several complicated conditions such as environment temperatures and different angles of indenter. In addition, the real thickness of the interface adhesion is difficult to determine. This thesis simplified these conditions by several methods, for example, by doing parameter normalization and assuming a unit thickness for interface in order to simulate the crack at interface with zero thickness.

The objectives of this research are:

1. To explore how to use the finite element simulation software – ABAQUS with the cohesive zone model to study the initiation and propagation of the delamination crack at the thin film/substrate interface during the nanoindentation.

2. To establish an FEM model with cohesive zone model for analyzing wedge indentation of thin film, and to develop a general methodology to determine interface strength and interface energy through the wedge indentation experiments

3. To study the effects of film thicknesses, material properties of the film and the substrate, and indenter geometries on the interfacial delamination

based on the simulation.

4. To predict the critical indentation load and critical indentation depth for the initiation of the delamination crack at the interface during the wedge indentation experiments.

1.2 Nano Indentation Experiment

Nano-indentation is a powerful experimental technique to determine the mechanical properties of materials at submicron to nanometer scales. These properties include hardness and elastic modulus. Nanoindentation technique was developed in early 1980s by Pethica et al. [1]. The basic analysis of the nano-indentation was first developed by Doerner and Nix in 1986 [2], and later on modified by Oliver and Pharr in 1992 [3].

During the nano-indentation tests, the penetration depth is in the order of nanometers to microns. The load-penetration curve is recorded continuously during indentation experiments, and such curve can be used to derive important mechanical parameters, such as hardness and elastic modulus. For most bulk materials the values of elastic modulus are consistent with those obtained by standard tensile testing. In this thesis, nano-indentation experiments using wedge sharp indenter are simulated using FEM method to determine the value of interface adhesion strength, critical failure load, and critical displacement for interfacial delamination during nano-indentations.

This thesis includes six chapters. After this introduction chapter, related

literature studies are summarized in Chapter 2. The literature studies include two parts, indentation theory and cohesive zone model. Chapter 3 describes the finite element modeling of the wedge indentation using ABAQUS with the cohesive zone model. Chapter 4 discusses the simulation results and the main factors affecting the simulation and the simulated results are compared with experimental results in Chapter 5. Finally conclusions and recommendations for future work are summarized in Chapter 6.

REFERENCES:

[1]. J.B.Pethica, R.Hutchings and W.C.Oliver, Philos. Mag. A, 48, 593 (1983).

[2]. M.F.Doerner and W.D.Nix., J. Mater. Res., 1, 601, (1986).

[3]. W.C.Oliver and G.M.Pharr, J.Mater. Res., 7, 1564, (1992).

Chapter 2 Literature Review

2.1 Theories of Indentation

2.1.1 Hardness

Hardness is one of the commonly-measured mechanical properties by indentation experiments. There are three main categories of hardness by different measuring methods: scratch hardness, indentation hardness and dynamic hardness [1].

The scratch hardness indicates the ability of one solid to be scratched by another. The scratch experiment is simple but it is complicated in theory therefore the scrach hardness can not be easily defined [2]. Indentation hardness is determined by the load and the corresponding size of the permanent impression formed in static indentations. Dynamic hardness is expressed in terms of either the height of rebound of the indenter, or the energy of impact and the size of the remaining indentation, which makes the number of the test variables beyond manageable level.

Hertz [3] was the first one to relate the absolute value of hardness with the least value of the pressure beneath a spherical indenter. Then Auerbach [4], Meyer [5] and Hoyt [6] developed various measurements and theory, finally the definition of hardness is generally accepted as:

$$H = \frac{P_{\max}}{A} \tag{2.1}$$

where H is the hardness, P_{max} is the maximum load of the indenter and A

represents the projected contact area of the specimen at the maximum load.

2.1.2 Nanoindentation

Nano-indentation is a later development of the indentation technique. It is commonly used to determine the mechanical properties of thin film/substrate systems. It has the capability to make the indentation at small load range, such as millinewton range and be able to measure the very small deformation created by the indentation, usually in the order of nanometers to microns.

In the conventional macro/micro indentation experiments, it is needed to measure the contact area using microscopes, which usually leads to errors in the measurement because of the small contact area and the elastic recovery during the unloading process. On the contrary, nanoindentation technique can record the load and the corresponding penetration depth continuously with high resolution. Hence, the direct measurement of contact area is not necessary. Therefore nanoindentation technique will get more accurate results in terms of load and penetration depth. In addition, the elastic modulus and hardness of the specimen can be obtained from the analysis of the experimental obtained load and penetration depth data.

2.1.3 Introduction to the theories of Wedge Indentation

Hill et al. [7] gave a theoretical analysis for an experiment in which elastic-plastic material is penetrated by a rigid and frictionless wedge. This

analysis based mainly on two assumptions:

1. The material is incompressible
2. The material is rigid until the yield strength is reached.

Hill tested lead specimens indented by sharp steel indenters with the largest semi-angle of 30^o and the results correlated with his theory well [7]. This theory was further proved by Dugdale [8]. Later on, Grunzweig [9] presented a solution for an indentation with a rough wedge indenter following Hilll's theory. The major difference is that the slip lines do not meet the wedge face at 45° when the wedge is rough and the effect of friction increases the apparent indentation pressure depending on the angle of the wedge tip and the coefficient of friction between the wedge tip and the specimen. Based on theory of indentation test on elastic-perfectly-plactic solid, Tabor [10] proposed the relationship of the mean contact pressure and the yield strength of the material:

$$p_m = CY \tag{2.2}$$

where P_m represents the mean contact pressure, Y is the yield strength, and C is a constant around 3. Later on Mulhearn [11] found that different angles of indenters might also contribute to the results of indentation tests. For example, if the semi-angle of the indenter is less than about 30°, Hill's theory works well, but when it exceeds 30° there should be another theory to explain the mechanism. When the indenter tip angle is lager than 30°, the deformation field can be approximated as a radial compression centered at the bottom of

the indenter. Marsh [12] further linked Mulhearn's mechanism to a cavity in an elastic-plastic material being expanded by internal pressure. He found that the elastic modulus of material played a critical role in this deformation mechanism. When the value of the ratio of elastic modulus to yield strength E/Y is high, the material would be amenable to radial compression and change easily under radial flow mechanism of deformation. Under the same theory, Hirst and Howse [13] measured indentation pressure for various materials by using wedge indenters with different angles. Their result showed that there were four main types of deformation and Hill's theory for plastic rigid solid could be applied when the angle of wedge indenter was acute enough and the E/Y ratio of the material was high, for other situations the indentation pressure should be written in another relation:

$$\frac{p_m}{Y} = M + N\ln(E/Y) \tag{2.3}$$

where M is a constant related to the angle of wedge indenter and N is almost a constant when the angle of wedge exceeds 120°. For blunt wedges and highly elastic materials, elastic deformation happens and it could be modeled as an elastic solid indented by a rigid wedge. The pressure induced by the wedge indenter at a point x is therefore can be found as [14]:

$$p = \frac{E\cot\theta}{\pi\left(1-\nu^2\right)}\cosh^{-1}\left(a/x\right) \tag{2.4}$$

where x is the distance from the center of wedge indenter, a is the half-width of the indentation, θ is the semi-angle of wedge. The mean pressure p_m is

given by:

$$p_m = \frac{E \cot \theta}{2\left(1 - v^2\right)} \tag{2.5}$$

This elastic theory predicts the distribution of pressure and the mean pressure well, but the pressure within a narrow central band under the indenter is below the values it predicted.

In his famous work, Johnson [15] found that, for blunt wedge indenters and materials with a low ratio of elastic modules to yield strength, the indentation pressure correlated with a single parameter expressed as (E/Y) tan β, here β is the angle of inclination of indenter to the surface. Johnson modified the expanding cavity model by replacing the cavity with an incompressible hemispherical core expended by an internal pressure as shown in Fig (2-1) and Fig (2-2):

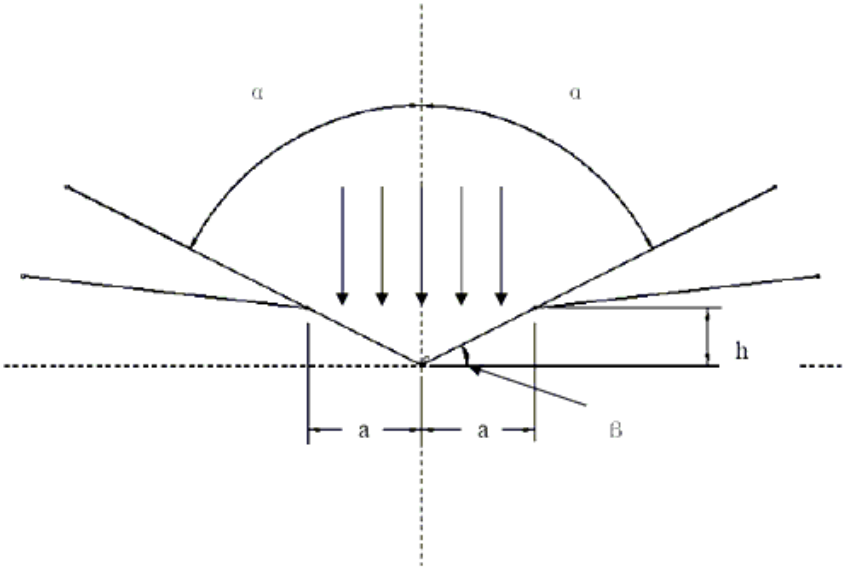

Fig 2-1 Schematic diagram showing the indentation of a surface by a rigid wedge tip.

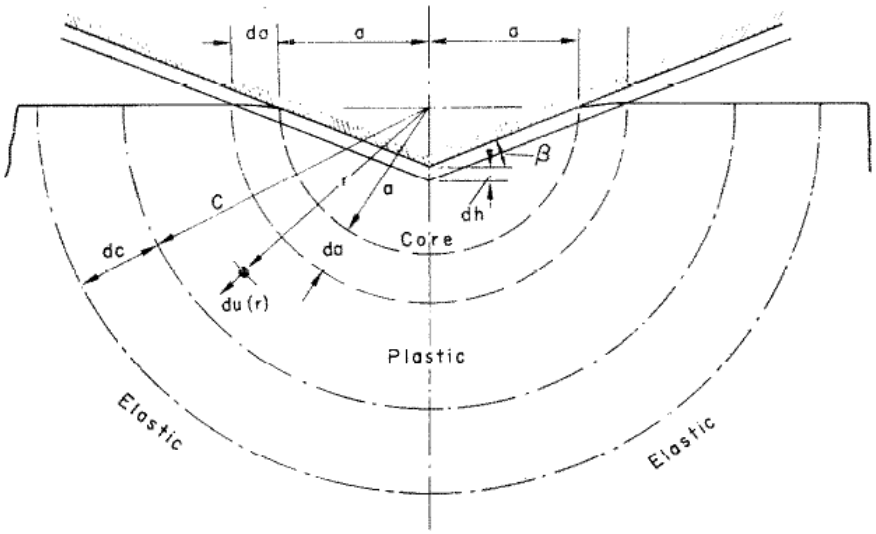

Fig 2-2 Idealized model of a hemispherical plastic 'core' attached to the indenter surrounded by a symmetrically deformed region [15]

In Johnson's model [15], similar to the case of an infinite elastic perfectly-plastic body with a cylindrical or spherical cavity under pressure, the pressure within the core was assumed to be hydrostatic, and the stress and displacement outside the core were assumed to be radial symmetric. The elastic-plastic boundary lies at a radius of c, and the radial stress and displacement were given:

$$\frac{\overline{p}}{Y} = -\left[\frac{\sigma_r}{Y}\right]_{r=a} = \frac{2}{\sqrt{3}}\left[\frac{1}{2} + \ln\left(\frac{c}{a}\right)\right] \tag{2.6}$$

$$\frac{du(r)}{dc} = \frac{2}{\sqrt{3}}\frac{Y}{E}\left[\frac{5-4v}{2}\frac{c}{r} - \frac{3(1-2v)}{2}\frac{r}{c}\right] \tag{2.7}$$

Neglecting the compressibility of the core, then:

$$\pi a du(a) = 2adh = 2a\tan\beta da \tag{2.8}$$

Substitute r = a into equation (2.7), dc/da = c/a, and then we obtain:

$$\frac{4E}{\pi Y}\tan\beta = (5-4v)\left(\frac{c}{a}\right)^2 - 3(1-2v) \tag{2.9}$$

From Eq.(2.6) and Eq.(2.9), we have:

$$\frac{\overline{p}}{Y} = \frac{1}{\sqrt{3}}\left\{1 - \ln(5-4v) + \ln\left[\frac{4E}{\pi Y}\tan\beta + 3(1-2v)\right]\right\} \tag{2.10}$$

If compressibility is neglected, the Poisson's ratio should be 0.5, therefore we obtain:

$$\frac{\overline{p}}{Y} = \frac{1}{\sqrt{3}}\left[1 + \ln\left(\frac{4}{3\pi}\frac{E}{Y}\tan\beta\right)\right] \tag{2.11}$$

This relation was obtained within small values of strain and β, however, the result agreed well with the experiments untill β=30°. Therefore, this relation is widely accepted and used in the analysis of wedge indentation experiments.

2.2 Introduction to Cohesive Zone Model

Perhaps one of the greatest achievements of continuum mechanics in the 20th century is that researchers can predict crack propagation in many media using fracture mechanics theory, such as the theory of Griffith's fracture for an ideal elastic material [16]. Linear elastic fracture mechanics (LEFM) predicts that the stress at the crack tip in a brittle material is singular and infinite [17],

which is physically unrealistic. It is Barenblatt [18] who first described fracture as a process of a material separation across a surface. This model appears by different names, such as cohesive process zone model, cohesive zone model, and so on. In recent years, the cohesive zone model has become one of the most popular models to simulate fracture in materials and structures. The cohesive zone model is originally applied to concrete and cementitious composites and interface fracture (see, for example, [19]). It is assumed that ahead of the physical crack tip, there is a cohesive zone which consists of upper and lower surfaces held by a cohesive traction. The cohesive traction is related to the separation displacement between the two surfaces. The relationship between the cohesive traction and the separation displacement can be called as “cohesive law” or “Traction-Separation law”. When an extended is force applied to the models, the upper and lower surfaces separate gradually, after the separation of these surfaces at the edges of the cohesive zone model reaches a critical value, the separation of the two surfaces leads to the crack growth. Although the cohesive zone model was originally proposed for model I fracture for the purpose of removing the crack tip stress singularity [20], it can also be applied in model III fracture process [17].

The necessary condition to eliminate stress singularity at the crack tip is that the cohesive traction must be a nonzero value at an initial vanishing separation displacement [21]. Additional fracture energy dissipation mechanism is needed besides the fracture process in cohesive zone when the

stress singularity exists at the cohesive zone tip. In general, the fracture energy in the cohesive zone model is the critical energy release rate in LEFM. This is true only if the cohesive zone is vanishingly small [22].

Although more complicated cohesive zone models can accurately simulate real material behavior, this also makes the solutions of the problems more difficult. One of the shortcomings, when using cohesive zone models is that one needs to predict the direction that cracks prefer to grow, such as that cracks growth occurs at material interfaces [23].

The cohesive zone model is now included in most of the finite element software packages, such as the general purpose finite element software – ABAQUS. ABAQUS offers a library of cohesive elements to model the behavior of adhesive joints, interfaces in composites, and other situations where the integrity and strength of interfaces may be of interest.

Fundamental Theory of Cohesive Elements Model at Interface

Broberg [24] depicted the appearance of the process zone in a cross-section normal to the crack edge by decomposing it into cells. The behavior of one single cell is defined by relationships between boundary loads and displacements conditions. If the cells are assumed as cubic and be put along the crack zone, this could be considered as a finite element in computations. Researches constructed cohesive models as that: tractions increase until a maximum, and then approach to zero when the separation displacement

increases. The thickness of the interface in the unloaded state is considered as zero. Tvergaard and Hutchinson [25] introduced traction-separation relation as following: let δ_n and δ_t be the normal and tangential components of the relative displacement of the respective faces across the interface in the zone (Fig. 2-3) [25-26]:

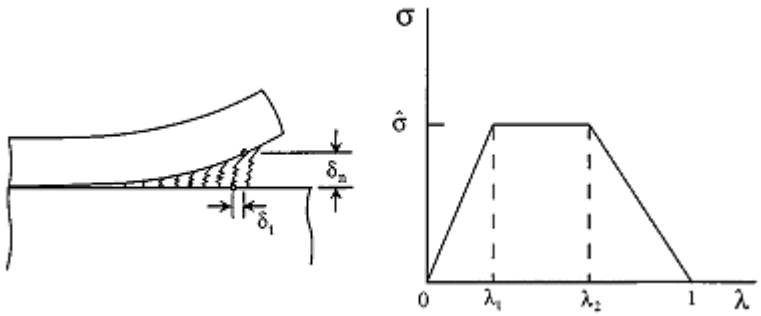

Fig 2-3 Traction-separation relation governing separation of the interface [26]

Then, a parameter λ is introduced to define the shape of the traction – separation law and it is defined as:

$$\lambda = \sqrt{\left(\delta_n / \delta_n^{\,c}\right)^2 + \left(\delta_t / \delta_t^{\,c}\right)^2} \tag{2.12}$$

The tractions are supposed to be zero when λ=1.

A potential from which the interface tractions in the separation zone are derived is defined as:

$$\Pi\left(\delta_n, \delta_t\right) = \delta_n^c \int_0^{\lambda} \sigma\left(\lambda'\right) d\lambda' \tag{2.13}$$

The normal and tangential components of the traction are given by

$$T_n = \frac{\partial \Pi}{\partial \delta_n} = \frac{\sigma(\lambda)}{\lambda}\frac{\delta_n}{\delta_n^c} \tag{2.14}$$

$$T_t = \frac{\partial \Pi}{\partial \delta_t} = \frac{\sigma(\lambda)}{\lambda}\frac{\delta_t}{\delta_t^c}\frac{\delta_n^c}{\delta_t^c} \tag{2.15}$$

If the tangential component of the traction is zero, the traction-separation law is a purely normal separation. This is the same case as the Mode I fracture. The peak normal traction under pure normal separation is termed the interface strength. The work of separation per unit area of interface is given by

$$\Gamma_0 = \frac{1}{2}\hat{\sigma}\delta_n^c\left[1-\lambda_1+\lambda_2\right] \tag{2.16}$$

The stress-strain relationship of the film material is assumed to be:

$$\varepsilon = \sigma / E \quad \text{for} \quad \sigma \le \sigma_Y \tag{2.17}$$
$$\varepsilon = \left(\sigma_Y / E\right)\left(\sigma / \sigma_Y\right)^{1/N} \quad \text{for} \quad \sigma > \sigma_Y$$

Studies in interface by applying cohesive zone model always contain the following parameters [26]:

$E, \nu, \sigma_Y, N, t(\text{film})$;
$E_s, \nu_s\,(\text{substrate})$;
$\Gamma_0, \hat{\sigma}(\text{interface})$

Generally, for mode I cohesive zone models, it only contains opening mode fracture, the relationship between the cohesive traction and the separation displacement could be expressed as:

$$\sigma = \sigma_c f\left(\delta / \delta_c\right) \tag{2.18}$$

In equation (2.18), σ_c is the peak traction, δ_c is a characteristic separation displacement, and f is a dimensionless function which relates to the shape of the cohesive traction-separation displacement curve (Fig. 2-3).

Review of Mixed mode Cohesive Zone Model

For a mixed mode fracture, for instance, mode I and mode II, both separation displacements and cohesive surface tractions have normal and tangent components. The general mixed mode cohesive zone model can be written as:

$$\sigma_n = f\left(\delta_n, \delta_s\right), \sigma_s = f\left(\delta_n, \delta_s\right) \tag{2.19}$$

where the subscript "n" and "s" represents "normal" and "shear", respectively.

To obtain better functional forms of f_n and f_s, a cohesive energy potential is often used. Ortiz and Pandolfi [27] introduced an effective separation and effective traction as:

$$\delta_{eff} = \sqrt{\delta_n^2 + \eta^2 \delta_s^2}, \sigma_{eff} = \sqrt{\sigma_n^2 + \eta^{-2} \sigma_s^2} \tag{2.20}$$

where "η" is a coefficient which could be changed according to different weights of the mode I and mode II fracture. Under loading conditions, the effective traction can be derived from a cohesive energy potential by:

$$\sigma_{eff} = \frac{d\Phi\left(\delta_{eff}\right)}{d\delta_{eff}} \tag{2.21}$$

The cohesive tractions can be obtained by:

$$\sigma_n = \frac{\partial \Phi}{\partial \delta_n} = \frac{\sigma_{eff}}{\delta_{eff}} \delta_n, \sigma_s = \frac{\partial \Phi}{\partial \delta_s} = \eta^2 \frac{\sigma_{eff}}{\delta_{eff}} \delta_s \tag{2.22}$$

Tvergaard and Hutchinson [25] used a different form of the shape function and found that the traction-separation relations are similar. On the other hand, Needleman [28], Xu and Needleman [29] didn't use the effective quantities, they considered that the cohesive potential was a direct function of two separations [28]:

$$T_n = -\frac{\partial \phi}{\partial u_n}, T_t = -\frac{\partial \phi}{\partial u_t} \tag{2.23}$$

Zhang and Deng [17] provided an effective approach to simulate Mode III crack. They found that the von Mises effective stress in the cohesive zone was a constant. The cohesive zone is a traction region in which the surface traction smoothly changes from zero at the crack tip to a certain magnitude at the cohesive zone tip. It was said that the cohesive zone was a mathematical extension of the crack and physical fracture process zone as shown in Fig. 2-4. Traction-separation relation therefore takes the form of [17]:

$$\sigma_{zy} = \tau_{\max} \left[1 - \left(\delta_z / \delta_{tip} \right)^{2/3} \right]^{1/2}, \left(0 \le \delta_z \le \delta_{tip} \right) \tag{2.24}$$

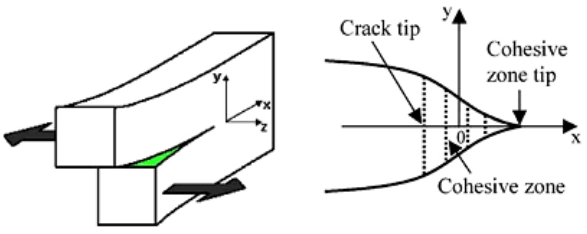

Fig 2-4 A schematic of a Mode III crack containing a cohesive zone ahead of the crack tip. [17]

For the Mode III crack, the von Mises effective stress in the cohesive zone could be written as:

$$\sigma_e = \sqrt{3\left(\sigma_{zx}^2 + \sigma_{zy}^2\right)} = \sqrt{3}\tau_{\max} \tag{2.25}$$

Therefore, the von Mises effective stress is a constant. Zhang and Deng [17] considered the von Mises effective stress as the yield stress of the surrounding bulk material.

Discussion on Cohesive Curve Shape in Cohesive Zone Modeling

Since Needleman [30] introduced the cohesive zone models in computational practice, cohesive zone models have become more and more frequently used in finite element simulations to solve the problem such as crack tip fracture and creep; crazing in polymers; adhesively bonded joints; interface cracks in bimaterials; delamination in composites and multilayers; fast crack propagation in polymers and so on. Most researchers considered the work of separation per unit area of interface and the strength of the interface as the two most important parameters in cohesive zone model [25-26, 31], and these results indicated that the shape parameters (or the shape of the traction-separation curve, Fig 2-3) have a relatively small influence. However,

Volokh [32] pointed out that a specific shape of the cohesive curve could essentially affect numerical simulation of the fracture process, which suggested that it was not enough to simulate interface fracture process by only considering the strength and separation work. There are different cohesive traction-separation shape functions such as these proposed by Needleman [28], Tvergaard and Hutchinson [25], Ortiz [27], Geubelle and Baylor [33]. All of the traction-separation shape functions can be classified into four main types [32]: (1) multilinear, (2) polynomial, (3) trigonometric, and (4) exponential as shown in Fig.2-6 to Fig.2-9. Volokh [32] performed block-peel tests (Fig.2-5) to examine the effects of the difference shapes of cohesive curves. He used Δ to represents the separation displacements in cohesive zone models and T to represents the tractions. T_{max} was the maximum surface traction which could also called cohesive strength. The corresponding separation displacement was Δ_{max}, and then he introduced the dimensionless parameters as shown in Equation (2.26):

$$\sigma = \frac{T}{T_{\max}}, \delta = \frac{\Delta}{\Delta_{\max}} \tag{2.26}$$

The work of separation is therefore:

$$J = \int T d\Delta \tag{2.27}$$

To be dimensionless, J is normalized by the product of T_{max} and Δ_{max}:

$$\phi = \frac{J}{T_{\max}\Delta_{\max}} \tag{2.28}$$

For a bilinear cohesive zone model, the traction-separation law has the

form:

$$\sigma = \begin{cases} \delta, & 0 \le \delta \le 1 \\ 2-\delta, & 1 \le \delta \le 2 \\ 0, & 2 \le \delta \end{cases} \qquad (2.29)$$

$$\phi = 1$$

For a parabolic cohesive zone model, it takes the form:

$$\sigma = \begin{cases} 2\delta - \delta^2, & 0 \le \delta \le 2 \\ 0, & 2 \le \delta \end{cases} \qquad (2.30)$$

$$\phi = 4/3 \cong 1.333$$

For a sinusoidal cohesive zone model:

$$\sigma = \begin{cases} \sin\left(\pi\delta/2\right), & 0 \le \delta \le 2 \\ 0, & 2 \le \delta \end{cases} \qquad (2.31)$$

$$\phi = 4/\pi \cong 1.273$$

For an exponential cohesive zone model:

$$\sigma = \delta e^{1-\delta},\ 0 \le \delta$$
$$\phi = \mathrm{e} \equiv \exp(1) \cong 2.718 \qquad (2.32)$$

Fig. 2-6 to Fig. 2-9 show the traction-separation curves (σ-δ curves) for the four cohesive zone models proposed by Volokh [32].

The peel test by Volokh [32] can be illustrated as in Fig. 2-5 and the results of the four types of the traction-separation forms are summarized in Table 2-1

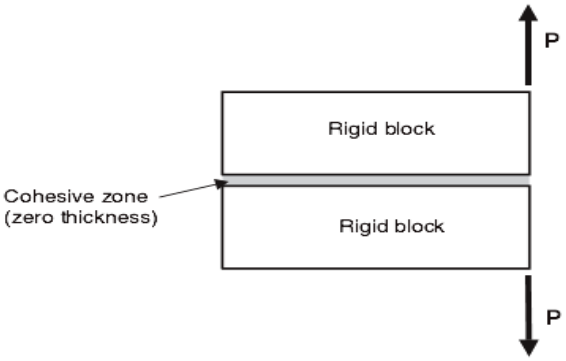

Fig 2-5 The peel test used by Volokh to study the effects of the cohesive curve shapes. [32]

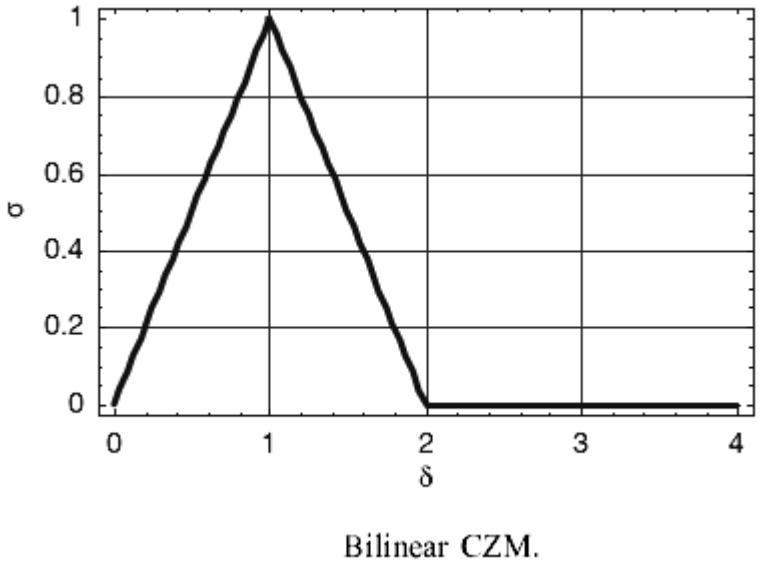

Fig 2-6 σ - δ curve for bilinear cohesive zone model [32]

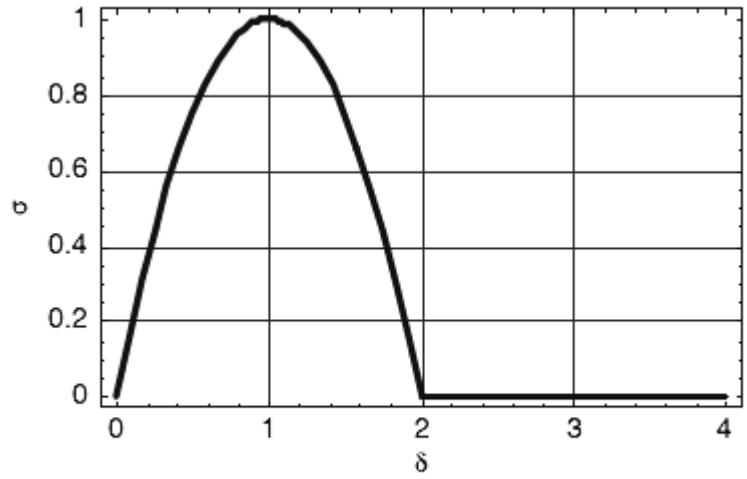

Fig 2-7 σ - δ curve for parabolic cohesive zone model [32]

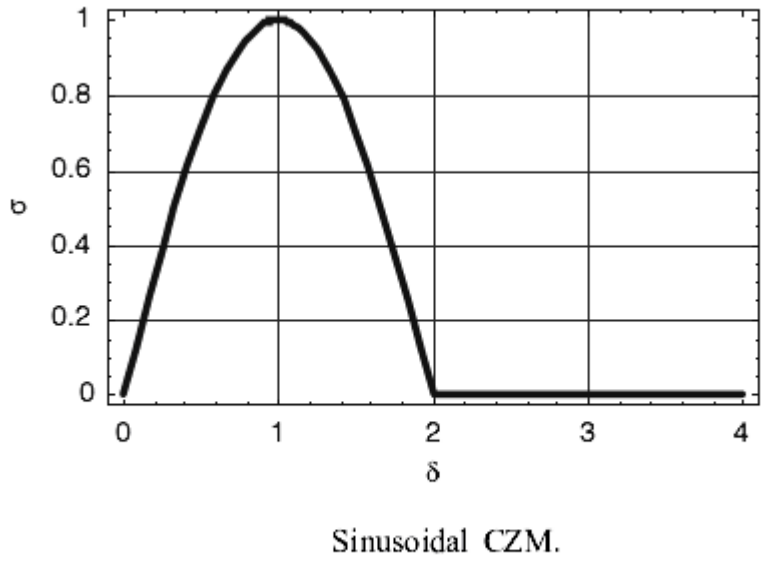

Fig 2-8 σ - δ curve for sinusoidal cohesive zone model [32]

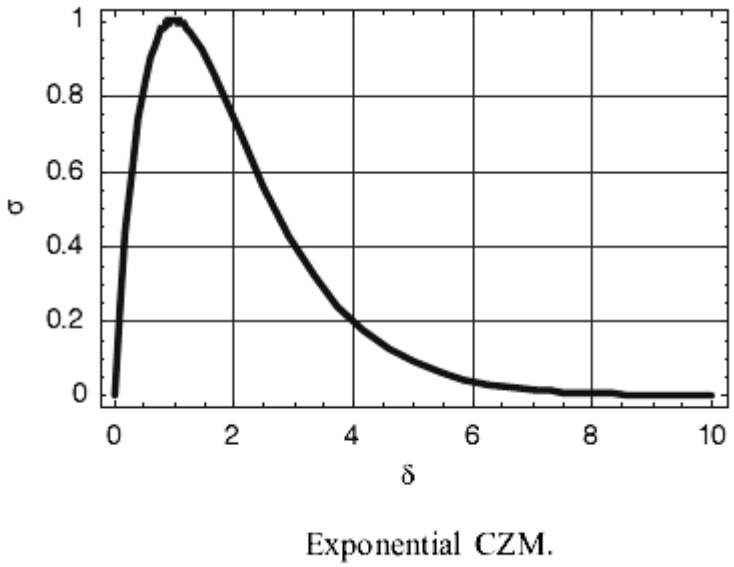

Fig 2-9 σ - δ curve for exponential cohesive zone model [32]

The calibrated parameters shown in Table 2-1 indicated that there were indeed differences in the work of separation, *J,* maximum surface traction, T_{max} and corresponding separation, Δ_{max}, due to the different shapes of the cohesive curves. Therefore, the shape of the traction-separation law may also have a significantly effects on the crack initiation and propagation processes. Recent numerical simulations by Chandra et al [34] also discovered the shape-sensitivity of cohesive zone models in elastic-plastic compliant body.

Three-dimensional Cohesive Zone Model in Finite Element Method

This part will discuss the general concept of building a three-dimensional cohesive zone model. In the three-dimensional model, the tractions and

separation displacements have three components. One is in the normal direction while the other two are in the shear directions. The traction-separation law is also provided as follow [35]:

For a rate independent cohesive zone model:

$$
\begin{aligned}
T_p &= \alpha_p \left(\frac{27}{4}\right)\sigma_{\max}\left(\frac{[u_p]}{\delta_p}\right)\left(1-2\lambda+\lambda^2\right), \\
T_n &= \left(\frac{27}{4}\right)\sigma_{\max}\left(\frac{[u_n]}{\delta_n}\right)\left(1-2\lambda+\lambda^2\right), \\
T_s &= \alpha_s \left(\frac{27}{4}\right)\sigma_{\max}\left(\frac{[u_s]}{\delta_s}\right)\left(1-2\lambda+\lambda^2\right),
\end{aligned}
\tag{2.33}
$$

where T_n, T_p, and T_s are coupled to both normal and tangential crack opening displacements. λ is the normalized quantity coupling normal and tangential behavior:

$$
\lambda = \sqrt{\left(\frac{[u_p]}{\delta_p}\right)^2 + \left(\frac{[u_n]}{\delta_n}\right)^2 + \left(\frac{[u_s]}{\delta_s}\right)^2}
\tag{2.34}
$$

where δ_n, δ_p and δ_s are material properties which are length scales associated with debonding, α_p and α_s are material properties relating shear to normal strength. When $\lambda>=1$, the values of tractions become zero, which indicates that the cohesive zone is fully debonded. The local coordinate system about the three-dimensional cohesive zone model is shown in Fig 2-10:

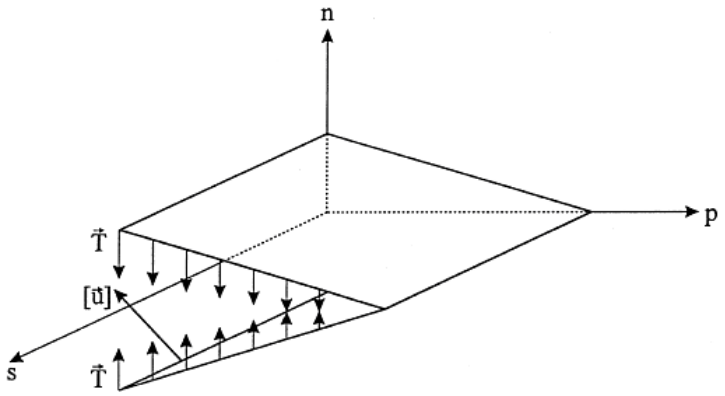

Fig 2-10 Local coordinate system for three-dimensional cohesive zone element [23]

For the rate dependent cohesive zone model, Tvergaard has pointed out the importance of including rate dependence in the cohesive zone model, in such case, the traction-separation law could be the following form [35]:

$$T_i = \frac{\left[u_j\right]}{\delta_j}\frac{\left[1-\alpha(t)\right]}{\lambda}\left[\sigma_i^f + \int_0^t D_{ij}(t,\tau)\frac{\partial\lambda}{\partial\tau}d\tau\right] \tag{2.35}$$

In equation (2.35), α is a damage parameter representing the microscopic dissipation mechanisms in the cohesive zone. It is an internal state variable governed by an evolution law [36]:

$$\frac{d\alpha}{dt} = a(1-\alpha)^m(1-\lambda)^n, \quad a \geq 0, m \geq 1, n \leq -1. \tag{2.36}$$

REFERENCES:

[1] H. O'Neill, Hardness Measurement of Metals and Alloys, Chapman & Hall, London, 1967.

[2] A.C. Ficher-Cripps, Nanoindentation, Springer-Verlag, New York, 2002.

[3] H. Hertz, J.Reine Angew. Math, 92 (1881) 156.

[4] F. Auerbach, Ann. Phys. Chem., 43 (1891) 61.

[5] E. Meyer, Phys. Z. 9 (1908) 66.

[6] S.L. Hoyt, Tans. Am. Soc. Steel Treat., 6 (1924) 396.

[7] R. Hill, E. H. Lee and S. J. Tupper, Proc. R. Soc. London, A188 (1947) 273.

[8] D. S. Dugdale, J. Mech. Phys. Solids, 2 (1953) 14.

[9] J. Grunzweig, I. M. Longman and N. J. Petch, J. Mech. Phys. Solids, 2 (1954) 81.

[10] D. Tabor, The Hardness of Metals, Clarendon Press, Oxford, 1951.

[11] T. O. Mulhearn, J. Mech. Phys. Solids, 7 (1959) 85.

[12] D. M. Marsh, Proc. R. Soc. Lond. A, Math. Phys. Sci., 279 (1964) 420.

[13] W. Hirst and M. G. J. W. Howse, Proc. R. Soc. Lond., A, Math. Phys. Sci., 311 (1969) 429

[14] I. N. Sneddon, Fourier Transforms, McGraw-Hill, New York, 1951.

[15] K. L. Johnson, J. Mech. Phys. Solids, 18 (1970) 115

[16] A.A. Griffith, Phil. Trans. Roy. Soc. Lond., A221 (1920) 163

[17] W. Zhang, and X. Deng,, Engineering Fracture Mechanics, 72 (2005) 1818

[18] G.I. Barenblatt, Journal of Applied Mathematics and Mechanics, 23 (1959) 434.

[19] Z. H. Jin, and C. T. Sun, Engineering Fracture Mechanics, 72 (2005) 1805

[20] G.I. Barenblatt, Adv Appl Mech, 7 (1962) 55

[21] Z.H. Jin, and C.T. Sun, Int J Fract., 134 (2005) 91

[22] C.Y. Wang, and C.T. Sun, ECCOMAS 2004, Jyvaskyla, Finland, (2004) 24

[23] J.W. Foulk, D.H. Allen and K.L.E. Helms, Comput. Methods Appl. Mech. Engrg., 183 (2000) 51

[24] K.B. Broberg, Cracks and fracture, San Diego, CA: Academic Press; (l999).

[25] V. Tvergaard, and J.W. Hutchinson, J Mech Phys Solids, 41 (1993), 1119

[26] Y. G. Wei, and J. W. Hutchinson, International Journal of Fracture, 93 (year) 315

[27] M. Ortiz, and A. Pandolfi, Int J Numer Meth Engng, 44 (1999) 1267

[28] A. Needleman, J Mech Phys Solids 38, (1990) 289

[29] X.P. Xu, and A. Needleman, J Mech Phys Solids, 42, (1994) 1397

[30] A. Needleman, Journal of Applied Mechanics, 54 (1987) 525

[31] V. Tvergaard, and J. W. Hutchinson, J. Mech. Phys. Solids, 40 (1992) 1377

[32] K. Y. Volokh, Commun. Numer. Meth. Engng, 20 (2004) 845

[33] P.H. Geubelle, and J. Baylor, Composites Part B Engineering, 29, (1998) 589

[34] N. Chandra, H. Li, C. Shet, and H. Ghonem, International Journal of Solids and Structures, 39, (2002) 2827.

[35] V. Tvergaard, Mater. Sci. Eng., A125 (1990) 203

[36] C. Yoon, and D.H. Allen, Int. J. Fracture, 96 (1999) 56

Chapter 3 Introduction to FEM Modeling of Wedge Indentations

3.1 Introduction

As discussed in the Section 2.2, linear elastic fracture mechanics (LEFM) predicts that the stress at a crack tip in a brittle material is singular and infinite, which is known as physically unrealistic, therefore a cohesive zone is introduced ahead of the crack tip, and the crack initiation which is difficult to investigate by using LEFM now can be studied by using cohesive zone model. Zhang et al [1] have used cohesive zone model to simulate the interface cracking initiation and propagation during a wedge indentation. Similarly, Li and Siegmund [2] used cohesive zone model to investigate a coating-substrate system with a conical indenter.

Jiang [3] has performed some detailed studies and extended the analysis developed by Zhang et al, as well as Li and Siegmund's work. A comprehensive simulation of the wedge indentation of the thin-film system has been developed, it also provided some fundamentals for current research work. However, following points are noticed for Jiang's work and these points also illustrated the differences between this work and previous one [3]:

- The thickness of film was relatively thick in Jiang's work (about 6 μm), therefore the simulation results might be difficult to compare with the experimental results, in which the film thickness is usually

less than 1 μm. It is expected that as the film thickness decreases, both the interface and film properties may change, therefore, in this work, we will focus on the thin films with thickness less than 1 μm.

- In Jiang's work, the substrate in thin film/substrate systems have a viscoelasticity behavior, therefore the simulation results might be different from the experimental results made on the low-k/Si system as for the low-k/Si system. Both low-k film and Si substrate are not viscoelastic. In the current work, the substrate is assumed to be elastic whereas the film is assumed to be elastic or elastic-plastic.
- In Jiang's work, the simulation used was a home-written FEM code, since cohesive zone model was not available in ABAQUS at that time.
- The shapes of the traction-separation curves are different. In ABAQUS, the cohesive curve is assumed to be bilinear triangle shape (Fig.2-6) and this is used in current analysis, however, in Jiang's work, the cohesive curve was assumed to be the shape similar to what is shown in Fig.2-3.
- In Jiang's work, the simulation was only performed for indenter angle of 120^{o}.

Therefore, in this work, a new simulation is established to couple with the nanoindentation experiments on low-k film/Si-substrate. The effects of film thickness, indenter length, film properties and indenter angles are studied. It

is also necessary to test the new version of ABAQUS with the cohesive zone model, and this will lay out some fundamental works for future research and simulation. One of the advantages to use cohesive zone model to simulate wedge indentation experiments is that there is no need to assume whether the interface is fully-bonded, partial bonded or pre-cracked. The interfacial delamination will occur once the damage criterion is met during indentation processes.

3.2 Methodology

In this project, the Finite Element Method (FEM) is employed to study the interface fracture mechanism of thin film/substrate system during wedge indentation. General purpose FEM models of thin film/substrate structure can be found in using ABAQUS/CAE. ABAQUS is an advanced general purpose FEM software, which provides complete and powerful solutions for routine and sophisticated linear and especially nonlinear engineering problems. Starting from version 6.5, ABAQUS includes a library of cohesive elements to model the behavior of adhesive joints, interfaces in composites, and other situations where the integrity and strength of interfaces may be of interest. This provides the possibility to use ABAQUS in this project.

3.3 Problem Formulation

For simplicity, in the FEM modeling, the wedge indenter is considered to

be rigid and frictionless, which means that the deformation of the indenter is neglected and there would be no friction force between the indenter and thin film/substrate systems. In addition, both indenter length and the width of thin film/substrate structure is assumed to be large enough (infinite long) so that the model could be considered as a two dimensional plane-strain case as shown in Fig 3-1

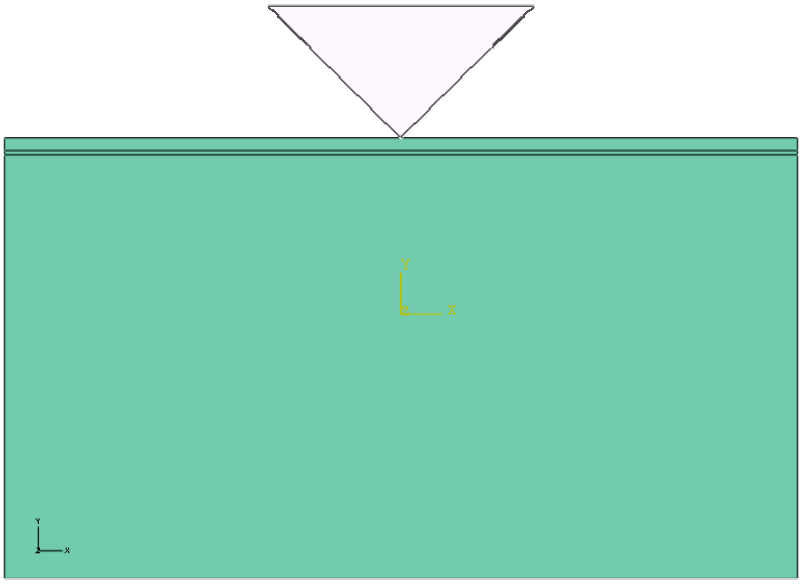

Fig 3-1 The geometry of the indenter tip and thin film/substrate system used for FEM simulations in this research.

Due to the symmetry of geometry and the assumption that the materials are isotropic, only half of the thin film/substrate system is taken into consideration during modeling. In addition, both the thin film and the substrate are assumed to be ductile enough so that the delamination along the interface will occur during the indentation.

During the interface delamination, the system is likely to undergo plastic deformation, linear elastic fracture mechanics predicts that the stress at the tip of a crack in a brittle material is singular and infinite, which is known as physically unrealistic. Therefore the traction-separation law is employed to study the fracture behavior of the interface. Generally it describes the fracture mechanism of the interface by a local stress-displacement relationship.

The FEM software ABAQUS has two analysis procedures, one of which is ABAQUS/Explicit and the other is ABAQUS/Standard. ABAQUS/Explicit is based on explicit FEM method, and ABAQUS/Standard is based on implicit FEM method. ABAQUS/Standard is more efficient for solving smooth nonlinear problems; on the other hand, ABAQUS/Explicit is the clear choice for a wave propagation analysis. The simulation work in this thesis mainly uses the implicit method by using ABAQUS/Standard.

The thin film/substrate system will be divided into three substructures: film, substrate, and the interface as shown in Fig 3-2. 4480 First-order (linear) interpolation Continuum plane strain elements (CPE4) and 9 Linear triangular elements of type CPE3 are applied in film and substrate structures, respectively, while 125 4-node cohesive elements (COH2D4) are applied in the interface (Fig.3-3).

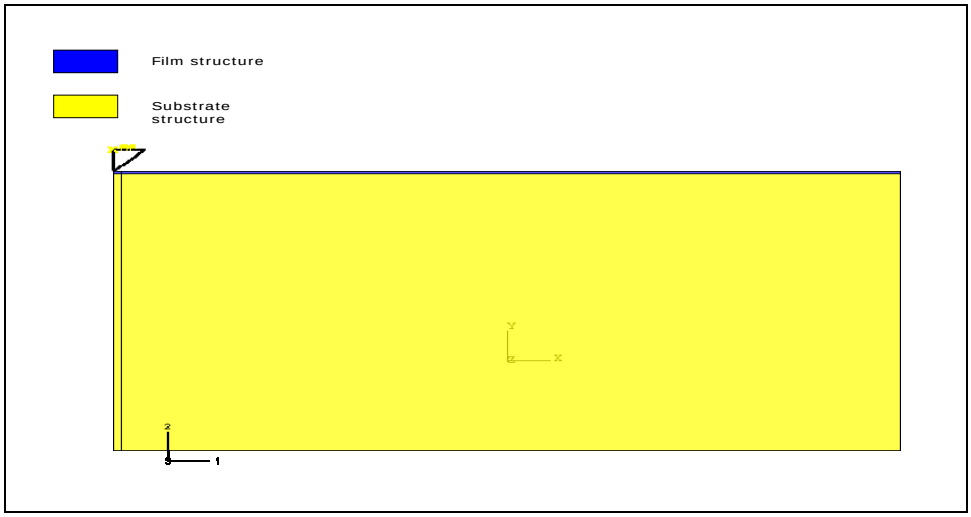

Fig 3-2 The Model of thin film/substrate system

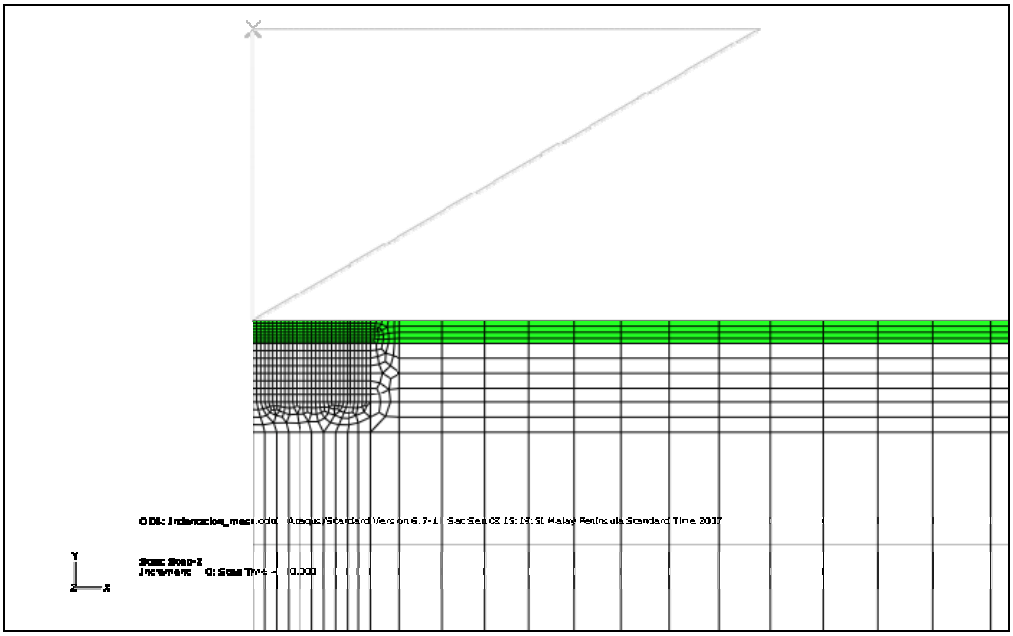

Fig 3-3 The structure of the mesh for the model of wedge indentation

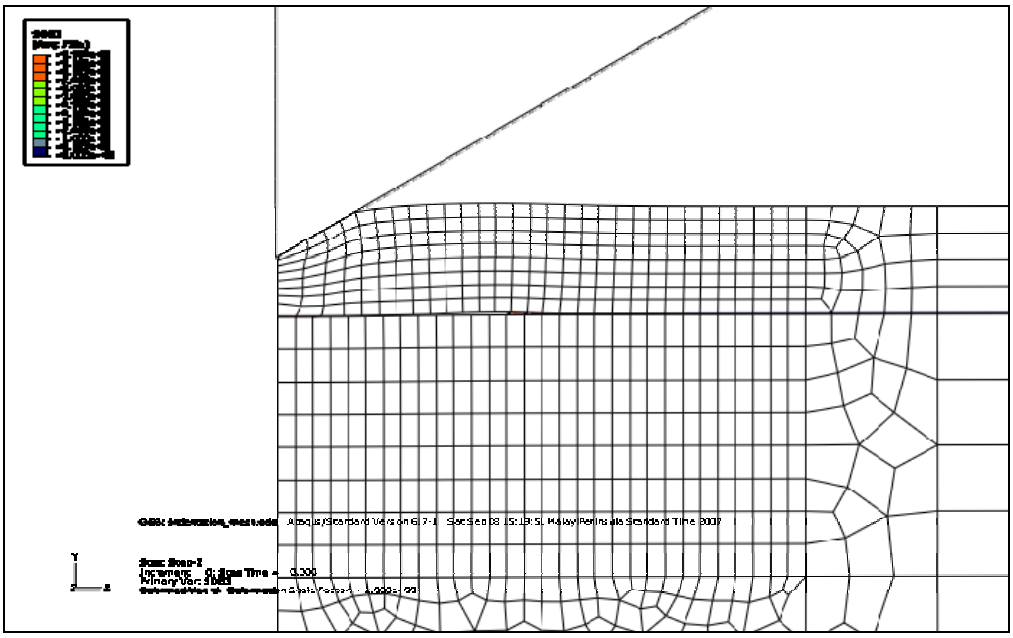

Fig 3-4 The deformation of the mesh during indentation and the initiation of the crack at the interface

Fig.3-4 and Fig.3-5 show the deformation of the mesh during indentation and the crack initiate at the interface when the indentation depth is approximately half of the film thickness. At this indentation depth, some of the cohesive elements finished the damage evolution progress, which means that the crack initiated. Fig.3-4 and Fig.3-5 also show that the crack initiates outside the contact area, and it doesn't initiate directly beneath the indenter tip.

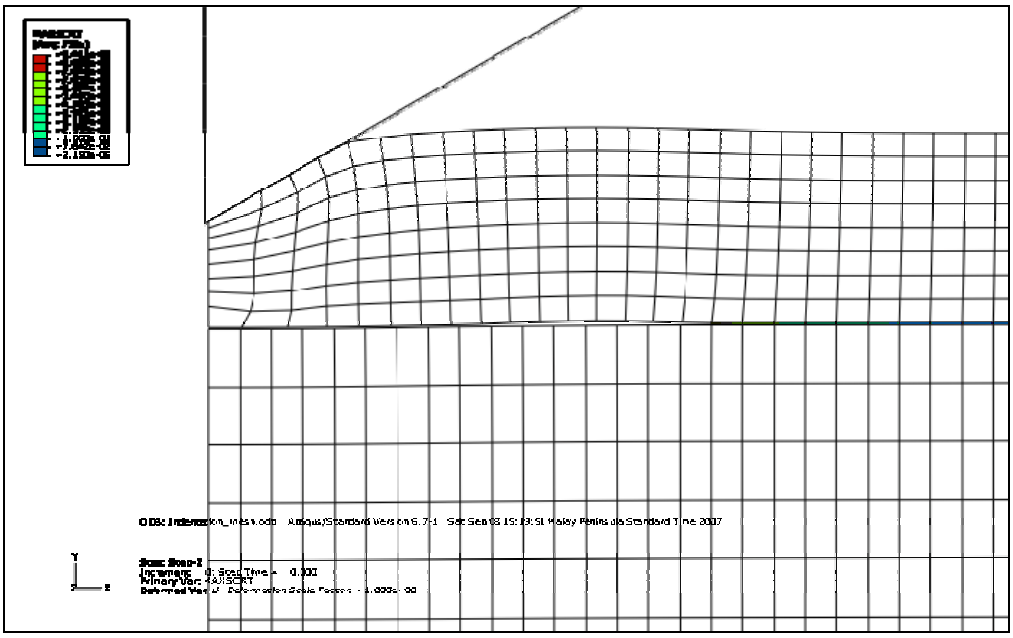

Fig 3-5 A close-looking of the deformation of the mesh during indentation and interfacial crack.

3.4 Introduction to Cohesive Element in ABAQUS

3.4.1 Overview

The constitutive behavior of the cohesive elements can be defined with a continuum-based constitutive model, a uniaxial stress-based constitutive model which is useful in modeling gaskets and/or single adhesive patches, or by using a constitutive model specified directly in terms of traction versus separation. In this work, the latter method is used for FEM modeling.

3.4.2 Cohesive Elements using a Traction-Separation Description

When the response of the cohesive elements is based on a traction-separation approach, ABAQUS assumes by default that the constitutive thickness is equal to 1.0. This default value is motivated by the fact that the geometric thickness of cohesive elements is often equal to (or

very close to) zero for the types of applications in which a traction-separation-based constitutive response is appropriate.

The available traction-separation model in ABAQUS assumes that the initially linear elastic behavior is followed by the initiation and evolution of damage, and the elastic behavior is expressed in terms of an elastic constitutive matrix that relates the nominal stresses to the nominal strains across the interface. In the calculations using cohesive zone model in ABAQUS, the nominal stresses are the force components divided by the original area at each integration point, and the nominal strains are the separations divided by the original thickness at each integration point. Therefore, normally the default value of the original constitutive thickness is settled to be 1.0, which ensures that the nominal strain is equal to the separation (i.e., relative displacements of the top and bottom faces). The constitutive thickness used for traction-separation response is typically different from the geometric thickness of the cohesive zone elements (which is typically close or equal to zero).

The nominal traction stress vector, t, consists of three components (two components in two-dimensional problems): t_n, t_s, and (in three-dimensional problems) t_t, which represent the normal (along the local 3-direction in three dimensions and along the local 2-direction in two dimensions) and the shear traction (two along the local 1- and 2-directions in three dimensions and one along the local 1-direction in two dimensions), respectively. In addition, the

corresponding separations are δ_n, δ_s, and δ_t. T_0 is the original thickness of the cohesive element, the nominal strains can be defined as:

$$\varepsilon_n = \frac{\delta_n}{T_0}, \varepsilon_s = \frac{\delta_s}{T_0}, \varepsilon_t = \frac{\delta_t}{T_0} \tag{3.1}$$

Then the elastic behavior of the interface can be written as:

$$t = \begin{Bmatrix} t_n \\ t_s \\ t_t \end{Bmatrix} = \begin{bmatrix} K_{nn} & K_{ns} & K_{nt} \\ K_{ns} & K_{ss} & K_{st} \\ K_{nt} & K_{st} & K_{tt} \end{bmatrix} \begin{Bmatrix} \varepsilon_n \\ \varepsilon_s \\ \varepsilon_t \end{Bmatrix} = \mathrm{K}\varepsilon \tag{3.2}$$

This elasticity matrix provides fully coupled behavior between all components of the traction vector and separation vector, and it depends on temperature and/or field variables. The off-diagonal terms in the elasticity matrix could be set to zero if uncoupled behavior between the normal and shear components is desired.

The material parameters of interface such as the interfacial elastic stiffness for a traction-separation model could be understood by studying the equation that represents the displacement of a truss of length L, elastic stiffness E, and original area A, due to an axial load P:

$$\delta = \frac{PL}{AE} \tag{3.3}$$

This equation can be rewritten as

$$\delta = \frac{S}{K} \tag{3.3}$$

where $S = P/A$ is the nominal stress and $K = E/L$ is the stiffness. The total mass of the truss, assuming a density ρ, is given by:

$$M = \rho AL = \overline{\rho} A \tag{3.4}$$

The equations above suggest that the actual length L could be replaced with the value 1.0 if the stiffness and the density are appropriately reinterpreted, which also ensures that the strain is the same as the displacement. In particular, the stiffness is $K = E/L$ and the density is $\overline{\rho} = (\rho L)$, where the true length of the truss is used in these equations. The density represents mass per unit area instead of mass per unit volume.

Likewise, these ideas could also be carried over to a cohesive layer of initial thickness T_c. If the adhesive material has stiffness E_c and density ρ_c, the stiffness of the interface is given by $K_c = (E_c / T_c)$ and the density of the interface is given by $\overline{\rho}_c = (\rho_c T_c)$. As discussed before, the default choice of the constitutive thickness for modeling the response in terms of traction versus separation is 1.0, regardless of the actual thickness of the cohesive layer because it is close to zero. Therefore in this situation the nominal strains are equal to the corresponding separations. When the constitutive thickness of the cohesive layer is "artificially" set to be 1.0, ideally only K_c and $\overline{\rho}_c$ (if needed) should be specified as the material stiffness and density, respectively, as calculated with the true thickness of the cohesive layer.

The discussion above provides a recipe for estimating the parameters required for modeling the traction-separation behavior of an interface in terms of the material properties of the bulk adhesive material. As the thickness of the interface layer is close to zero, the above equations imply that the stiffness,

K_c, tends to infinity and the density, $\overline{\rho}_c$, tends to zero. This stiffness is often chosen as a penalty parameter.

3.4.3 Damage Modeling

Damage of the traction-separation response is defined within the same general framework used for conventional materials. This general framework allows the combination of several damage mechanisms acting simultaneously on the same material. Each failure mechanism consists of three ingredients: a damage initiation criterion, a damage evolution law, and a choice of element removal (or deletion) upon reaching a completely damaged state. While this general framework is the same for traction-separation response and conventional materials, many details of how the various ingredients are defined are different. Therefore, the details of damage modeling for traction-separation response are presented below.

The initial response of the cohesive element is assumed to be linear as discussed above. However, once a damage initiation criterion is met, material damage can occur according to a user-defined damage evolution law. Fig 3-6 shows a typical traction-separation response with a failure mechanism. If the damage initiation criterion is specified without a corresponding damage evolution model, ABAQUS will evaluate the damage initiation criterion for output purposes only; there is no effect on the response of the cohesive element (i.e., no damage will occur). The cohesive layer does not undergo damage under pure compression.

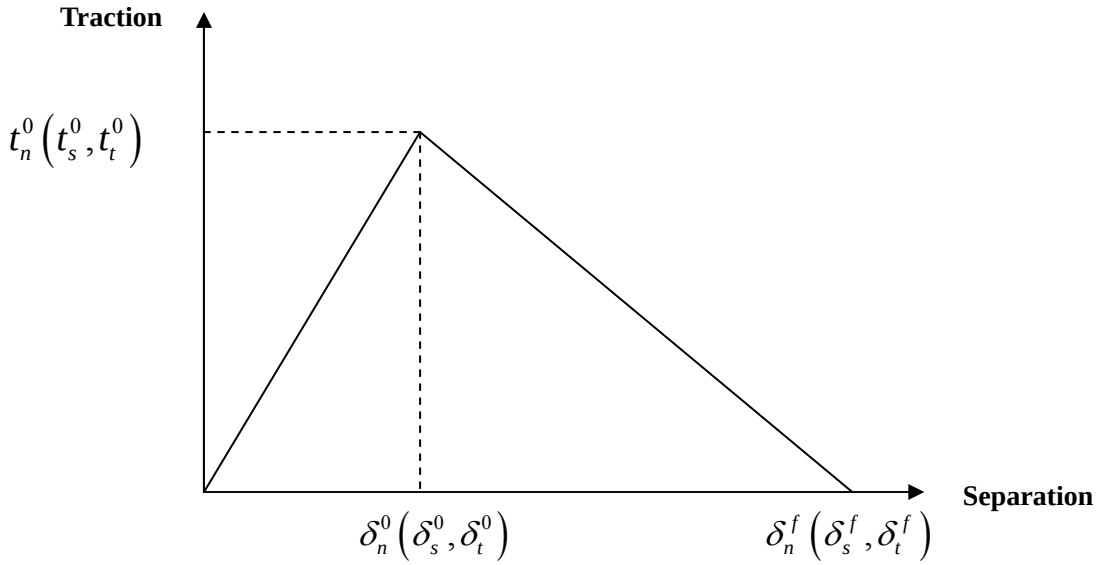

Fig 3-6 A typical traction-separation curve used for FEM simulation in this project.

$t_n^0\left(t_s^0,t_t^0\right)$ and $\delta_n^0\left(\delta_s^0,\delta_t^0\right)$ are the tractions and separations when the crack initiates, while $\delta_n^f\left(\delta_s^f,\delta_t^f\right)$ is the separations when the crack forms. When the tractions and separations reach the peak of Fig 3-6, the crack will initiate, and this crack will complete if the separations reach to the point $\delta_n^f\left(\delta_s^f,\delta_t^f\right)$.

REFERENCES:

[1] Y.W. Zhang, K.Y. Zeng, and R. Thampurun, Materials Science and Engineering, A319–321 (2001) 893

[2] W. Li and T. Siegmund, Acta Material, 52 (2004) 2989.

[3] H. Y. Jiang, Master thesis, Department of Materials Science, NUS, (2005).

Chapter 4 Modeling and Result

4.1 The Geometry

An FEM model is built to study the wedge indentation response of the thin film/substrate system, with the angle of the wedge indenter tip is 90°, due to the geometry symmetrical, only half of the indenter and material system is simulated.

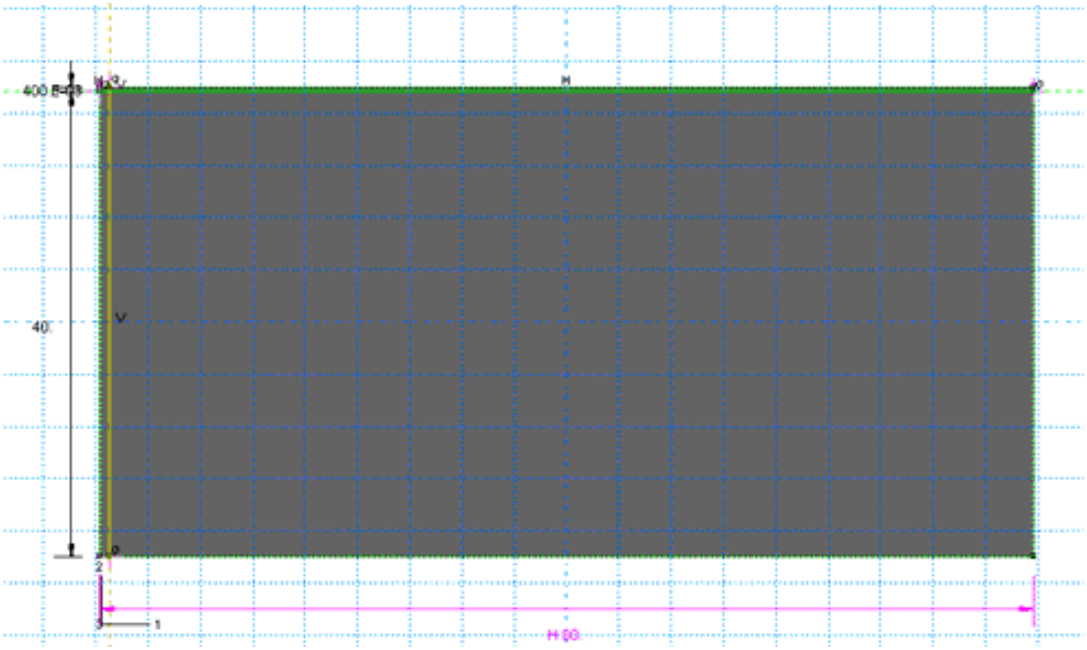

Fig 4-1 Geometry of the thin film/substrate system used in the FEM model.

As shown in Fig 4-1, the thickness of the film is 0.4 μm, and the thickness of substrate is 40 μm, while the thickness of the interface layer is assumed to be 0.004 μm. In fact during the simulation this thickness is considered as zero when compared with the thickness of film and the thickness of substrate,

which will be in accordance with the real situation. Fig 4-2 shows the geometry of the indenter. It can be seen that the height of the indenter is much larger compared to the thickness of the thin film, this is to ensure that the indenter can penetrate into the film and reach to the substrate.

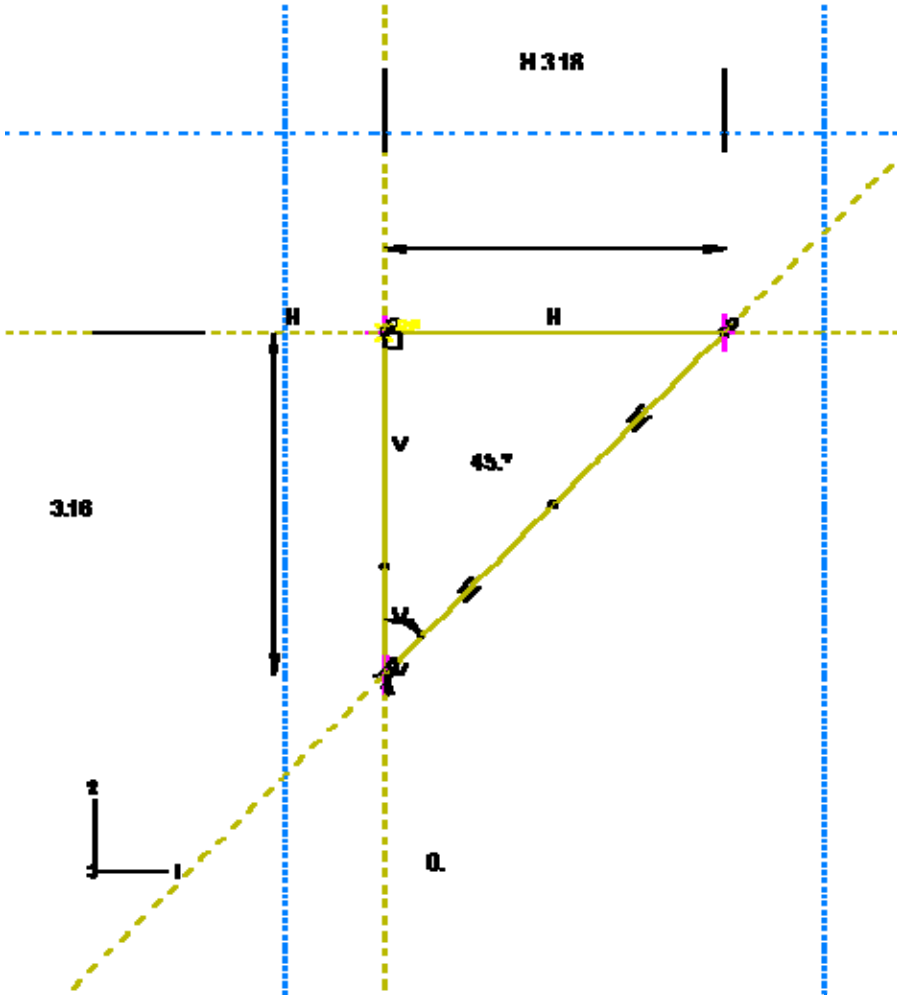

Fig 4-2 Geometry of the indenter used in the FEM model

4.2 The Material Properties of Film, Substrate and the Interface

The material properties of film and substrate are summarized in Table 4-1. These values are taken from the nanoindentation measurements on

low-k/Si-substrate system. (Thin film is Black Diamond BD film)

Table 4-1 Material properties of thin film and substrate

	Young's modulus E[GPa]	**Yield Stress [GPa]**	**Poisson's ratio**
Film	9.66	1.13	0.34
Substrate	112.4	3.10	0.28

The material property for interface is more complicated than those of the film and substrate. The damage initiation criterion for the interface in this case is defined by a parameter named MAXS: i.e. assuming that the damage is initiated when the maximum nominal stress ratio (as defined in the expression below) reaches to a value of one, i.e.

$$\max\left\{\frac{\langle t_n \rangle}{t_n^0}, \frac{t_s}{t_s^0}, \frac{t_t}{t_t^0}\right\} = 1 \tag{4.1}$$

In equation (4.1), t_n^0, t_s^0, and t_t^0 represent the peak values of the nominal stress when the deformation is either purely normal to the interface or purely shear in the first or the second direction, respectively. The symbol '$\langle\ \rangle$' used in the equation represents the Macaulay bracket with the usual interpretation. The Macaulay brackets are used to signify that a pure compressive deformation or stress state does not initiate damage.

In the simulation, the three stress components are set to be equal to each other with the value of 0.55 GPa.

The damage evolution criterion is based on energy, as a power law forms:

$$\left\{\frac{G_n}{G_n^C}\right\}^\alpha + \left\{\frac{G_s}{G_s^C}\right\}^\alpha + \left\{\frac{G_t}{G_t^C}\right\}^\alpha = 1 \tag{4.2}$$

The mixed-mode fracture energy is defined as $G^C = G_n + G_s + G_t$ when the above condition is satisfied. In Eq. (4.2) the quantities G_n, G_s, and G_t refer to the work done by the traction and its conjugate relative displacement in the normal, and the shear in the first, and the second directions, respectively. The quantities G_n^C, G_t^C and G_s^C refer to the critical fracture energies required to cause failure in these three directions, respectively.

For simplification, it is assumed that the power equals to 1.0 in Eq. (4.2). Therefore, the damage evolution criterion becomes:

$$\frac{G_n}{G_n^C} + \frac{G_t}{G_t^C} + \frac{G_s}{G_s^C} = 1 \tag{4.3}$$

In the simulation performed in this work, all the value of the three fracture energy is set to be 6 N/m, and the stiffness of interface is assumed to be 5,000 GPa.

In summary, for this FEM simulation, the strength of the interface is set to be 0.55 GPa, the fracture energy is set to be 6 N/m (the value from experiment is 5.5~6.5 N/m), and the stiffness of the interface is set to be 5,000 GPa. The

interface stiffness value is selected based on trial and error, it was found that this value did not affect the results significantly. However, if this value was set too small, then the computing work will not converge. It is believed that this is due to some bugs in ABAQUS software and need to be solved by the software company. Hence, the simulation results presented in this thesis are therefore based on these interfacial properties.

4.3 The Analysis Technologies for Simulation

This simulation work is performed on ABAQUS 6.6-1. The element type for thin film and substrate is CPE4 – 4-node linear plane strain element. Element type for interface is 4-node cohesive element COH2D4. The main output parameters include MAXSCRT and SDEG. MAXSCRT indicates whether the maximum nominal stress damage initiation criterion has been satisfied at a material point. It is evaluated as Equation (4.1). When MAXS reaches 1.0, it means that the damage initiate. SDEG is the overall value of the scalar damage variable. The parameter SDEG increases from 0.0 to 1.0, which stands for the damage evolution, and the evolution is finished when SDEG equals to 1.0, which means that the cohesive element is fully damaged and therefore a crack is formed.

4.4 The Interaction and the Boundary Conditions for the Case Study

It is assumed that there is no friction between the indenter and the thin

film/substrate system during the indentation test, so that we use frictionless interaction property in this case.

Fig 4-3 shows the boundary conditions for thin film/substrate systems, including follows:

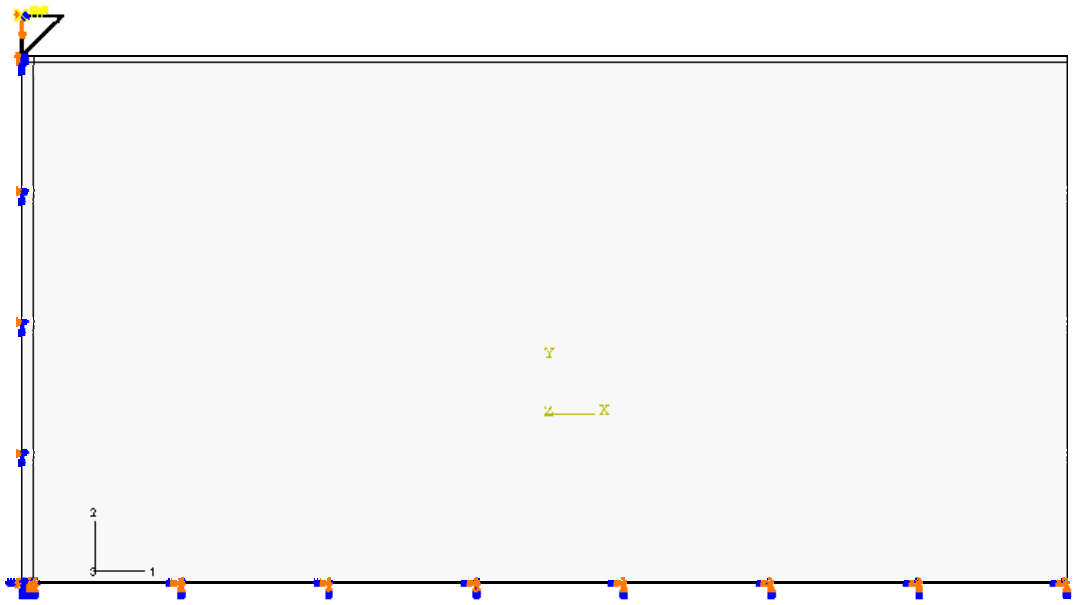

Fig 4-3 Boundary conditions used for the FEM model

- U1=U2=U3=UR1=UR2=UR3=0 (bottom)
- U1=UR2=UR3=0 (left edge)
- U1=U3=UR1=UR2=UR3=0, U2= 0.4 μm (indenter)

The value of displacement freedom U2 equals to the depth of the indentation during an indentation experiment.

4.5 Result Discussion

4.5.1 Indentation P-h Curves

An example of the FEM simulated indentation load-displacement curve

(P-h curve) is shown in Fig.4-4. It clearly shows that, there is a sudden decreasing load in the indentation P-h curve which reveals that the crack happens. With the further increase of the indentation depth, the slope of the P-h curve also decreased after the load change as shown in Fig 4-4. This result is consistent with what be found by previous student [1], and it is also known that the sudden decreasing load corresponds to the initiation of the interfacial crack [2].

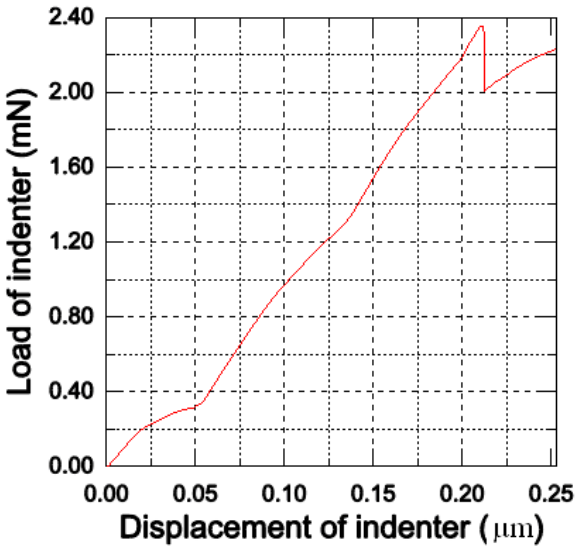

Fig 4-4 FEM simulated indentation load-penetration curve for 400 nm thickness film.

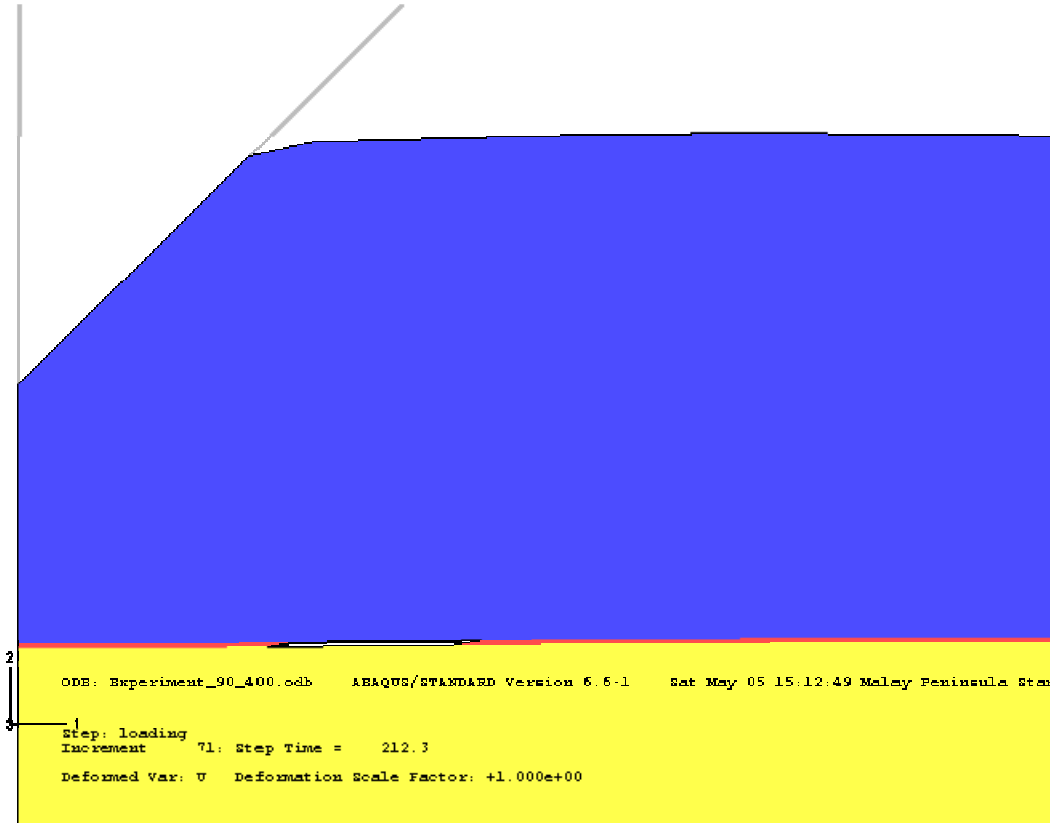

Fig 4-5 The FEM simulation with cohesive elements at the interface shows the crack formation at the indentation depth h=0.21 μm.

4.5.2 Interface Cracking

As discussed above, Fig 4-4 shows that at the time an interface crack initiates, there would be a significant decrease in the load in the load-penetration curve (P-h curve). Fig. 4.5 shows that an interface crack has initiated at this point. With the increase of the penetration depth, the delamination occurs at the interface, where the cohesive elements are located, the cracking causes the stiffness of the whole system to decrease significantly. Therefore, the P-h curve after the crack initiation shows significant lower stiffness as shown in Fig.4-4. This result provides the possibility that we could

identify when the crack is formed by studying the characteristic of the indentation P-h curve. However, it must be noticed that this simulation is under the condition of displacement control, whereas if the experiments are usually performed under load-control condition, the situation might be different.

4.5.3 The Position of the Delamination Cracks

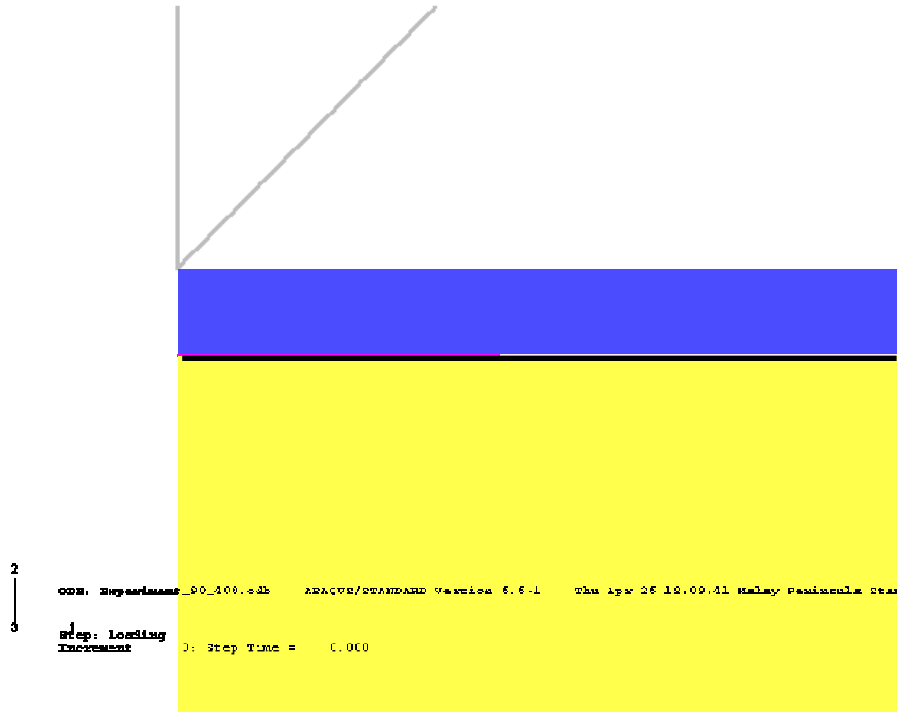

Fig 4-6 The geometry of cohesive zone model used for FEM simulation.

As shown in Fig 4-6, a path between the film and substrate is created along the cohesive element edge at the interface, which later will be used to study the distribution of stress field at interface and the place where crack may occur.

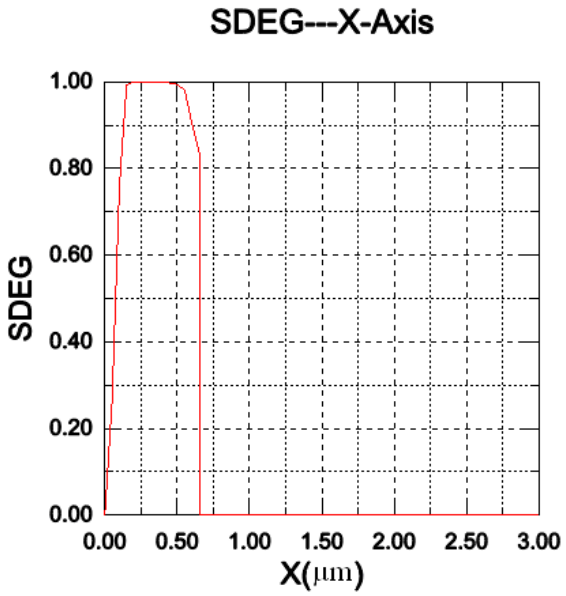

Fig 4-7 Value of SDEG (overall value of the scalar damage variable) along the interface (SDEG=1.0 indicated the position of the cracking).

Fig 4-7 shows the changes of the damage variable, SDEG, along the interface. The value SDEG = 1.0 indicates the damage of the interface, therefore a crack will occur at SDEG=1.0. Fig.4-7 shows that the crack may not occur right beneath the indenter tip, but occurs at approximately 0.1 to 0.5 μm from the center of the indenter tip. This position is just outside the contact zone by indenter tip. Similar result has also been reported previously by Zhang et al [2], and recently by Liu et al [3].

Fig 4-5 shows the possible position where crack may develop in this case. In this figure the cohesive element in which SDEG equal to 1.0 have been removed, therefore the general crack status can be seen. It is shown that, in general, the crack starts outside the contact zone when the indenter reaches to

approximately 50% of the film thickness. This agrees well with the experimental observations [4].

4.5.4 The Evolution of Traction along the Path

At the beginning of the delamination progress, the normal traction along the interface should be negative. With the penetration depth of the indenter increasing, the shear traction in direction 1 (shown in Fig. 4-5) along the interface reach a maximum value and then decrease to zero, at the same time, the normal stresses have negative values, which indicates that the damage initiation is mainly caused by shear stress and the crack is generally Mode II. This conclusion is supported by the result showed in Fig. 4-8, that the distribution of shear stress along interface at the moment when delamination happens, as well as the result showed in Fig. 4-9 for the distribution of the normal stress. In addition, according to the results showed in the Fig. 4-7 and Fig. 4-8, we can find that when the delamination happens at the interface, the shear stress at around 0.25 μm in x-axis is zero, and this position is where the interface crack started, the shear stress component increases along the interface, reaches to its maximum value ahead of crack tip. This suggested that the shear stress might also drive the initial propagation of the crack.

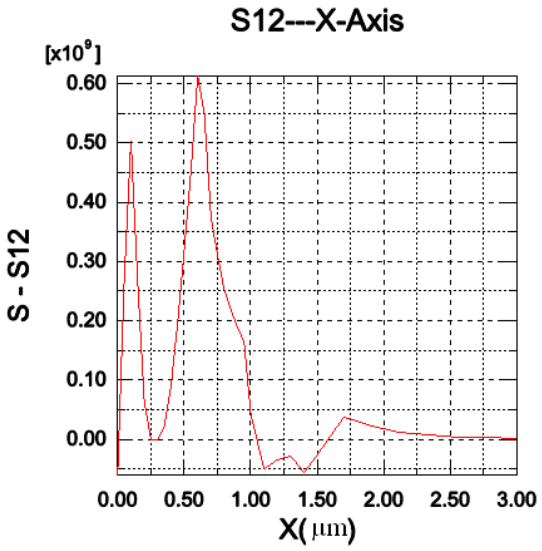

Fig 4-8 Shear stress component, S_{12} (Pa), along the interface. Noticed that the shear stress is zero at the beginning of the crack, and increases to a maximum value ahead of crack tip.

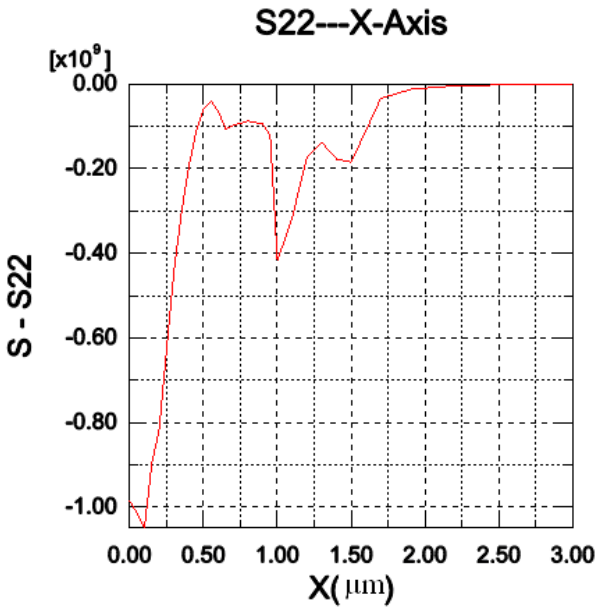

Fig 4-9 Normal stress component, S_{22} (Pa), along the interface. Noticed that the normal stress is negative along the crack position.

4.6 Nanoindentation of the Films with Different Thickness

4.6.1 Elastic Film case

Table 4-2 shows the values of D_c and P_c for thin film/substrate systems with different film thickness, where D_c is the critical indentation depth, which is the indentation depth when interface crack happens. P_c is the critical indentation load where the interface crack occurs. The film is assumed to be elastic with the elastic modulus of 9.66 GP_a (Table 4-1). Fig 4-10 and Fig 4-11 show that the critical indentation load (the load of indenter when damage initiate) and critical indentation depth (the depth of indenter when damage initiate) increased almost linearly with the increase of the film thickness. It is also noticed that the critical indentation load and depth for different film thicknesses are also in linear relation (Fig.4.12). This suggests that, at least within the range of the film thickness used in this simulation, the indentation load-displacement curves for different film thickness can be scaled. However, this conclusion is only for materials which could be considered as elastic.

Fig 4-13 to Fig 4-18 respectively show the load- penetration curves for the 6 thin film systems with different film thicknesses as listed in the Table 4-2. It can be seen that, for thicker film, the critical depth is larger, and to reach the deeper critical depth, obviously it will need higher critical indentation load. However, it is interesting to notice that the D_c and P_c increase linearly with film thickness when the film thickness changes from 0.5 μm to 1.0 μm. This

result may be due to the pure elastic behavior of the film and substrate in simulation, therefore the relationship of critical load, critical depth and film thickness become linear. Another possible reason is that the thickness of the film used in this simulation is below 1 μm, and for thicker films this linear relation may need to be re-examined. However, in all of the cases, the interfacial crack occurs at the indentation depth approaches to about half of the film thickness. This is in agreement with the experimental results reported by Yeap et al recently [4]. Another interesting feature can be found in these curves is that, the amount of decreasing load also increases with the film thickness. This could be related with the volume of the materials above the crack also increased with the film thickness. Yeap et al [4] has shown that the volume of the materials above the crack is actually related to the interface toughness, and this would need some more studies in the future.

Table 4-2 D_c and P_c for thin film/substrate systems with different film thicknesses

	film(μm)	interface(μm)	substrate(μm)	D_c(μm)	P_c(mN)
1	0.5	0.004	40	0.24	0.79
2	0.6	0.004	40	0.28	0.91
3	0.7	0.004	40	0.32	1.05
4	0.8	0.004	40	0.36	1.16
5	0.9	0.004	40	0.40	1.30
6	1	0.004	40	0.44	1.43

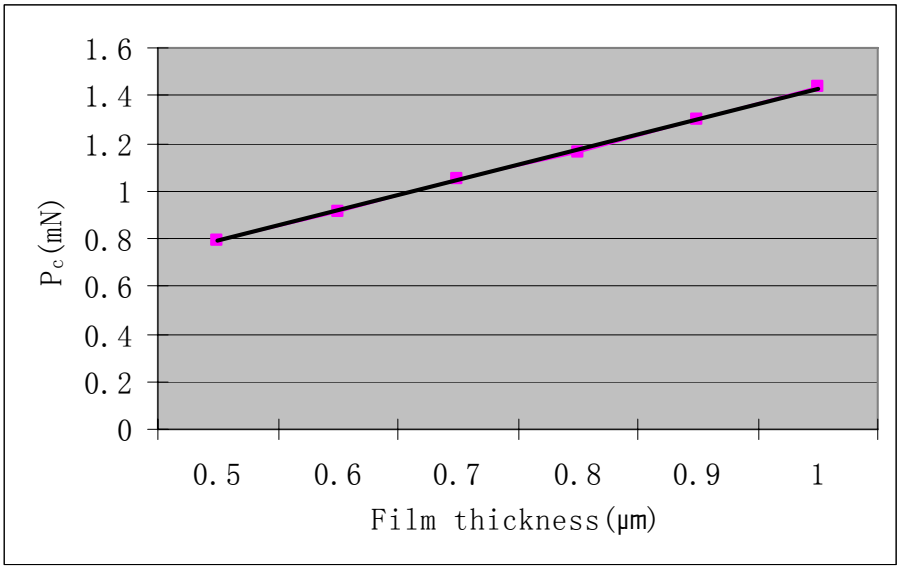

Fig 4-10 The values of critical indentation load, P_c, as function of the film thicknesses.

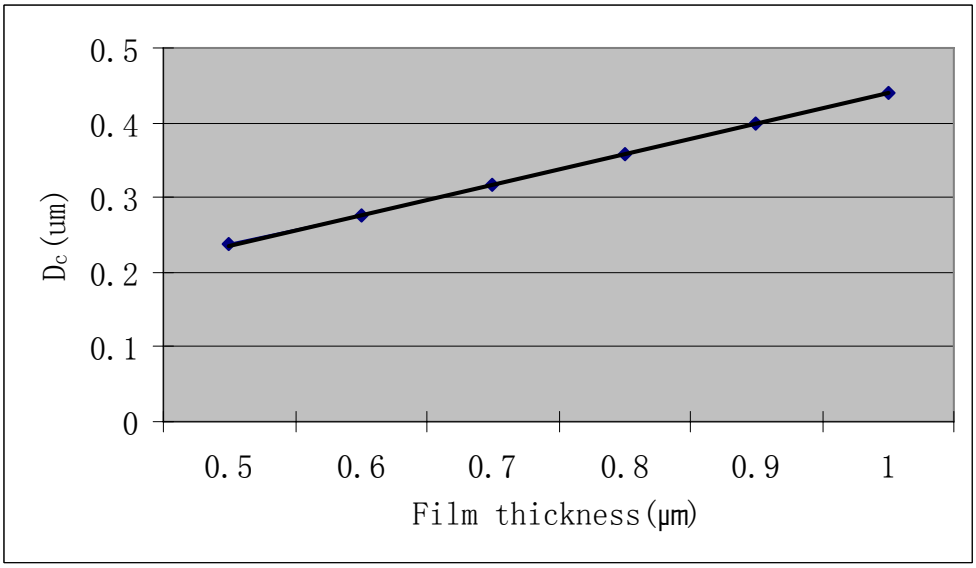

Fig 4-11 The values of the critical indentation depth, D_c, as function of the film thicknesses

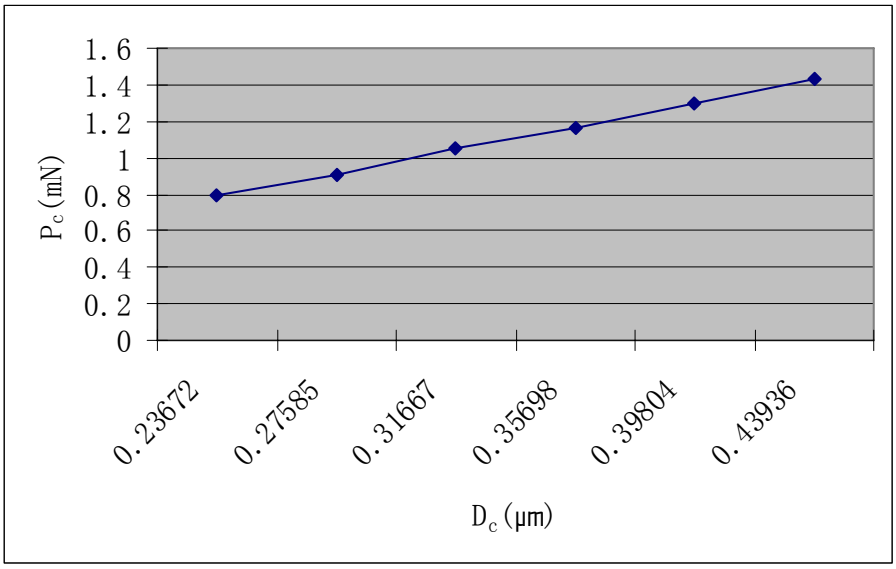

Fig 4-12 The values of critical indentation load, P_c, as function of the critical indentation depth, D_c, for different film thicknesses.

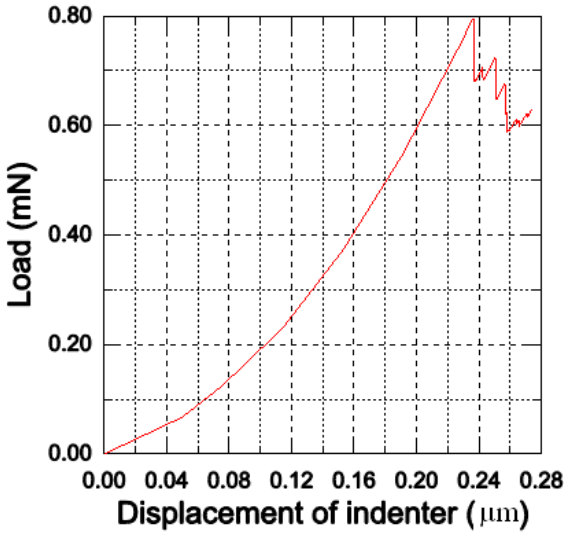

Fig 4-13 The FEM simulated load- penetration curve for thin film system with the thickness of 0.5 μm .

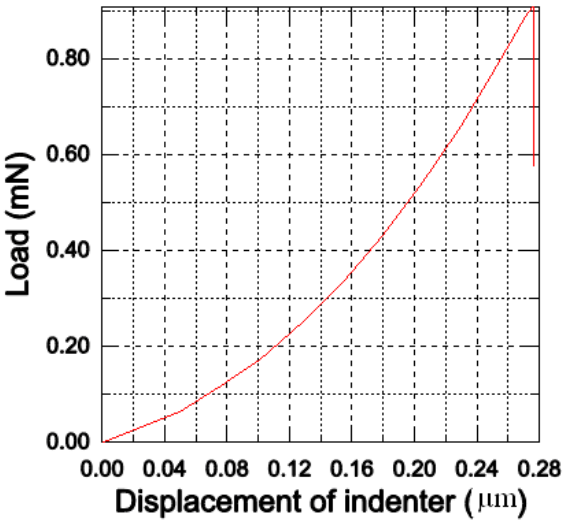

Fig 4-14 The FEM simulated load- penetration curve for thin film system with the thickness of 0.6 μm .

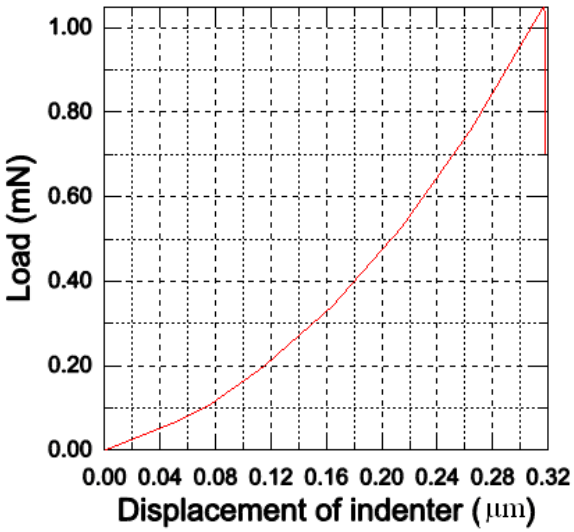

Fig 4-15 The FEM simulated load- penetration curve for thin film system with the thickness of 0.7 μm .

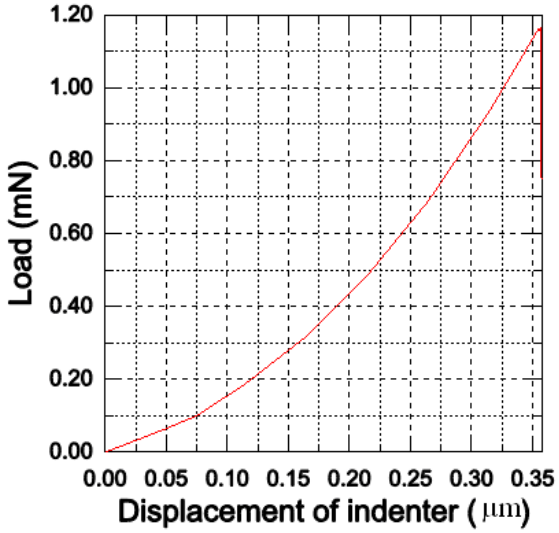

Fig 4-16 The FEM simulated load- penetration curve for thin film system with the thickness of 0.8 μm .

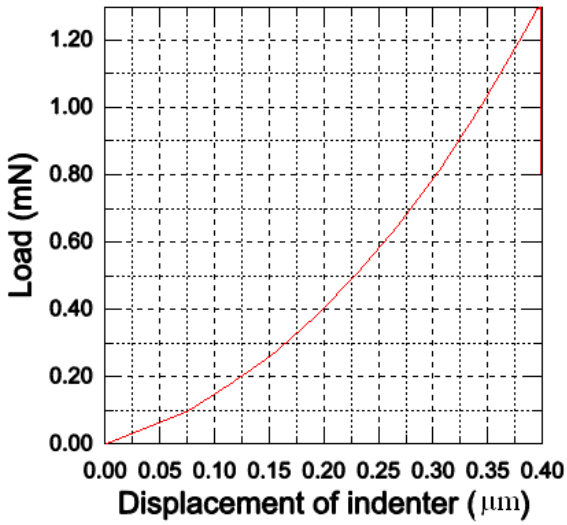

Fig 4-17 The FEM simulated load- penetration curve for thin film system with the thickness of 0.9 μm .

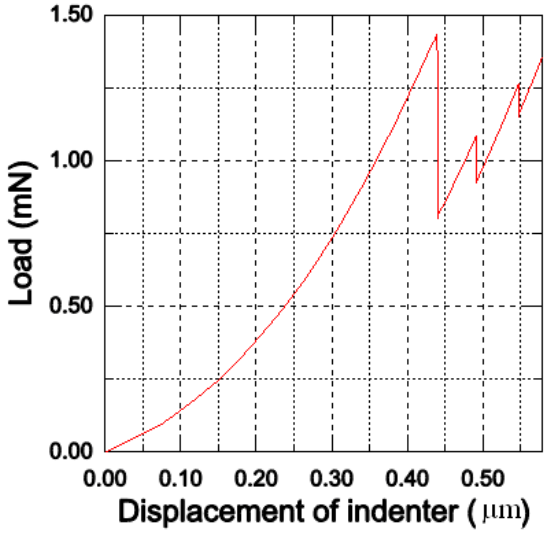

Fig 4-18 The FEM simulated load- penetration curve for thin film system with the thickness of 1.0 μm .

4.6.2 Film with Elastic-Plastic Behavior

Table 4-3 shows the critical indentation depth and the critical indentation load during indentation experiment on thin film/substrate systems in which the material properties of the film is assumed to be elastic-perfect-plastic (with the film yielding strength of 1.13 GPa, and elastic modulus of 9.66 GPa, Table 4-1). Fig 4-19 shows that the relationship between the film thickness and the critical indentation load is no longer a linear one, and so does the relationship of the film thickness and critical indentation depth. Fig. 4-20 to Fig. 4-25 show the load-penetration curves for each film thickness system.

As discussed in section 4.6.1, for thin film with pure elastic behavior, the relationship of critical load, critical depth and film thickness may be simpler

such as linear, however, for thin film with elastic-perfect-plastic behavior, this linear relationship does not exist any more. This may be because that after the indentation stress reaches to the yield stress of the film,, the energy of the thin film/substrate system will dissipate and the film will yield, which will have a significant influence on the critical indentation depth and critical indentation load, and therefore the plastic behavior affect the linear relationship.

Table 4-3 The critical penetration depth and the critical load for elastic-plastic cases

Film (μm)	Interface (μm)	Substrate (μm)	D_c(μm)	P_c(mN)
0.5	0.004	40	0.24	0.37
0.6	0.004	40	0.28	0.43
0.7	0.004	40	0.33	0.52
0.8	0.004	40	0.37	0.58
0.9	0.004	40	0.42	0.66

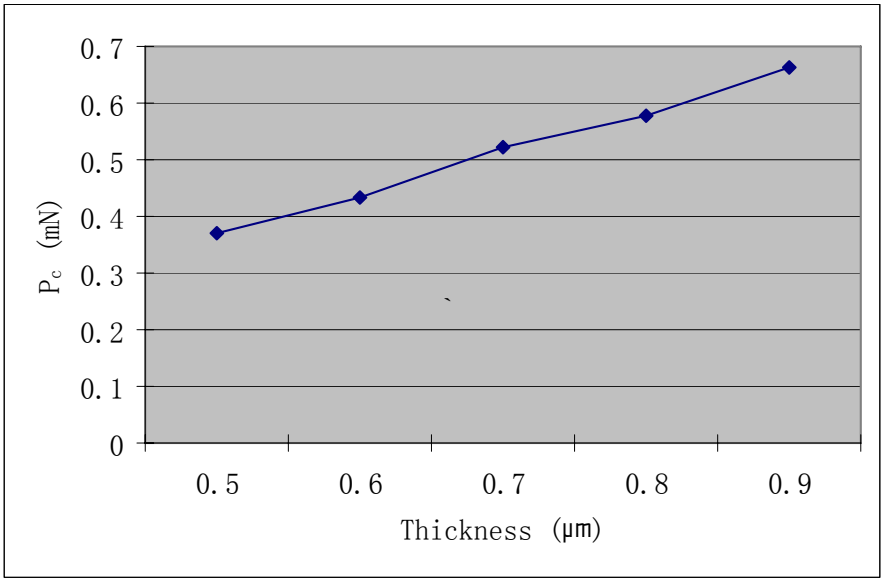

Fig 4-19 The values of critical indentation load, P_c, as function of film thicknesses for the case of film is elastic-perfect plastic.

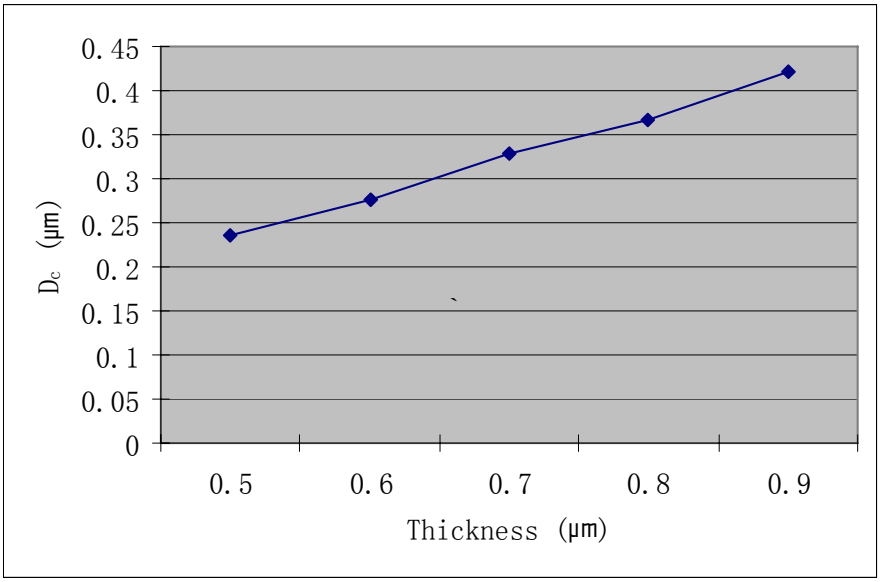

Fig 4-20 The values of critical indentation depth, D_c, as function of film thicknesses for the case of film is elastic-perfect plastic

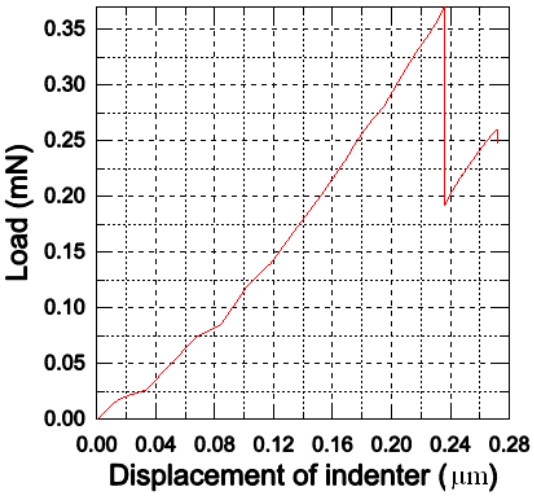

Fig 4-21 The FEM simulated indentation load- penetration curve for the thin film system with the thickness of 0.5 μm and the film is assumed elastic-perfect-plastic

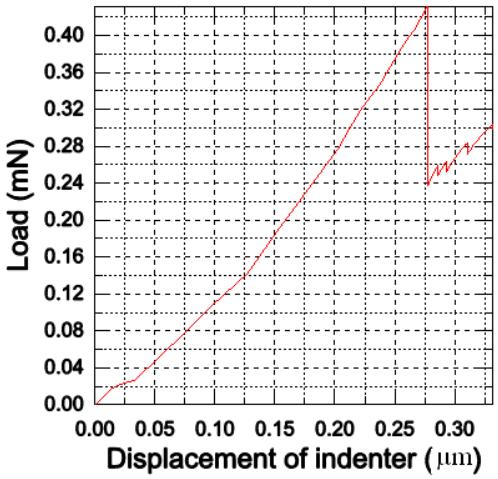

Fig 4-22 The FEM simulated indentation load- penetration curve for the thin film system with the thickness of 0.6 μm and the film is assumed elastic-perfect-plastic

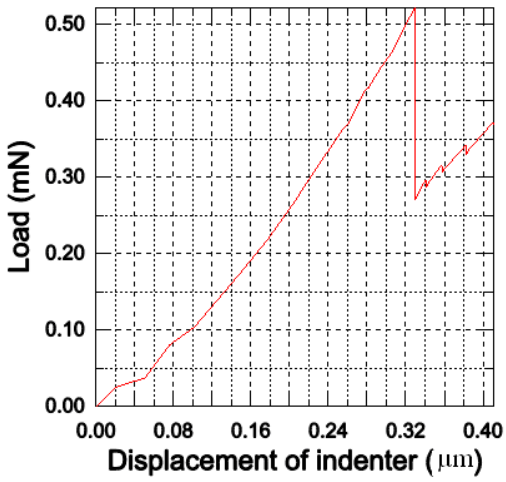

Fig 4-23 The FEM simulated indentation load- penetration curve for the thin film system with the thickness of 0.7 μm and the film is assumed elastic-perfect-plastic

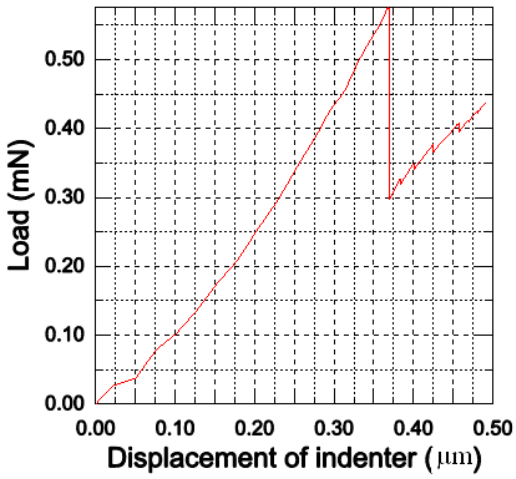

Fig 4-24 The FEM simulated indentation load- penetration curve for the thin film system with the thickness of 0.8 μm and the film is assumed elastic-perfect-plastic

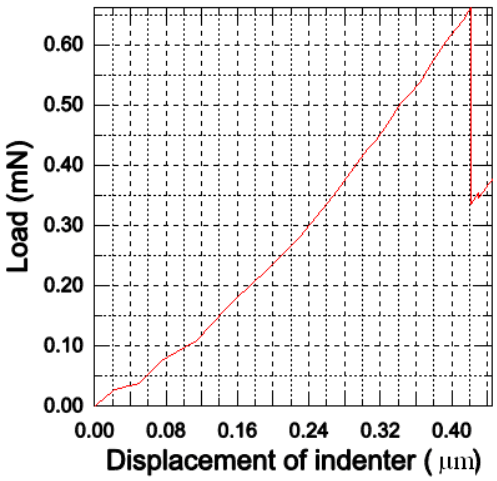

Fig 4-25 The FEM simulated indentation load- penetration curve for the thin film system with the thickness of 0.9 μm and the film is assumed elastic-perfect-plastic

Comparing the results presented in Table 2 and Table 3, although the interface properties are the same, it is found that the critical indentation depth at the interface delamination for the cases of the film to be purely elastic and elastic-perfect-plastic are almost the same, whereas the critical indentation load has been reduced significantly for the case of the film to be elastic-perfect-plastic. The critical indentation loads for the case of elastic-perfect-plastic films are less than 50% of those for the case of elastic films. This suggests that the film properties have significant effects on the critical indentation load for interface delamination, whereas little effects on the critical indentation depth. The interfacial delamination always occurs at the

indentation depth reaches to approximately 50% of the film thickness. For real film system, it may have certain strain hardening behaviors, therefore the critical indentation load should be in between the two cases simulated here.

4.7 Edge effect in Nano-indentation Experiment

4.7.1 Differences between the Simulation and Indentation Experiment

The result of simulation is mainly based on the assumption that both indenter and film are same width as shown in Fig 4-26(A), but the width of the tip or film is not considered during the simulation, therefore it can be considered as a plane strain condition. However, this is different form the real experimental situations of the wedge indentation of thin films as shown in Fig 4-26(B). In other words, simulation is a two-dimensional case where the indentation experiment is a three-dimensional case. Due to this difference the edge of the indenter may affect the stress and strain field significantly, in which the plane strain condition is not applicable to entire wedge length, but only same portion of the wedge length, most likely the middle part, to be under plane strain condition. This section will present a simple simulation to illustrate the effects of the wedge length on the critical indentation load and depth for the interface delamination.

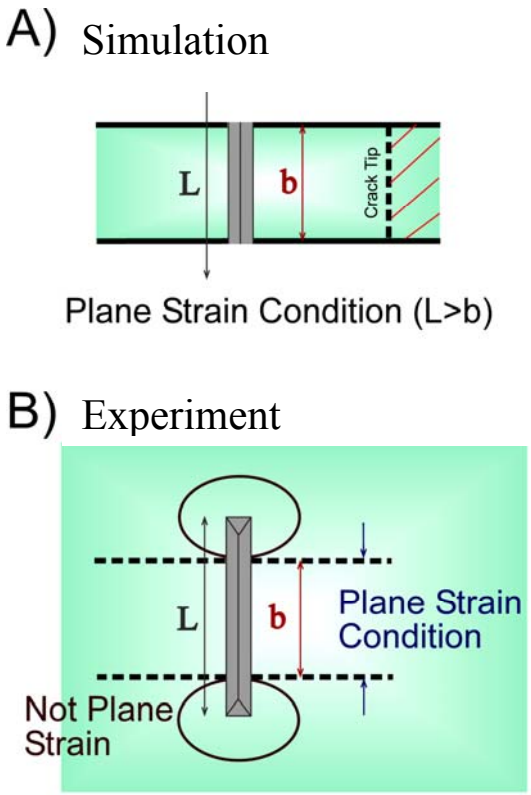

Fig 4-26 (a) FEM simulation of the wedge indentation of fine line structures (L>=b), and (b) Experimental wedge indentation of continuous film (L<<film width)

4.7.2 Effects of Plane Strain Conditions

The differences mentioned in Section 4.7.1 will be studied in this part for more detail. A simple model is built to study the middle section in indentation experiment on thin film/substrate systems. The model is shown in Fig 4-27. The yellow color is film while the blue area is substrate. In fact there is a red area between the film and substrate area, however, the thickness of the interface is too small to be seen in this figure.

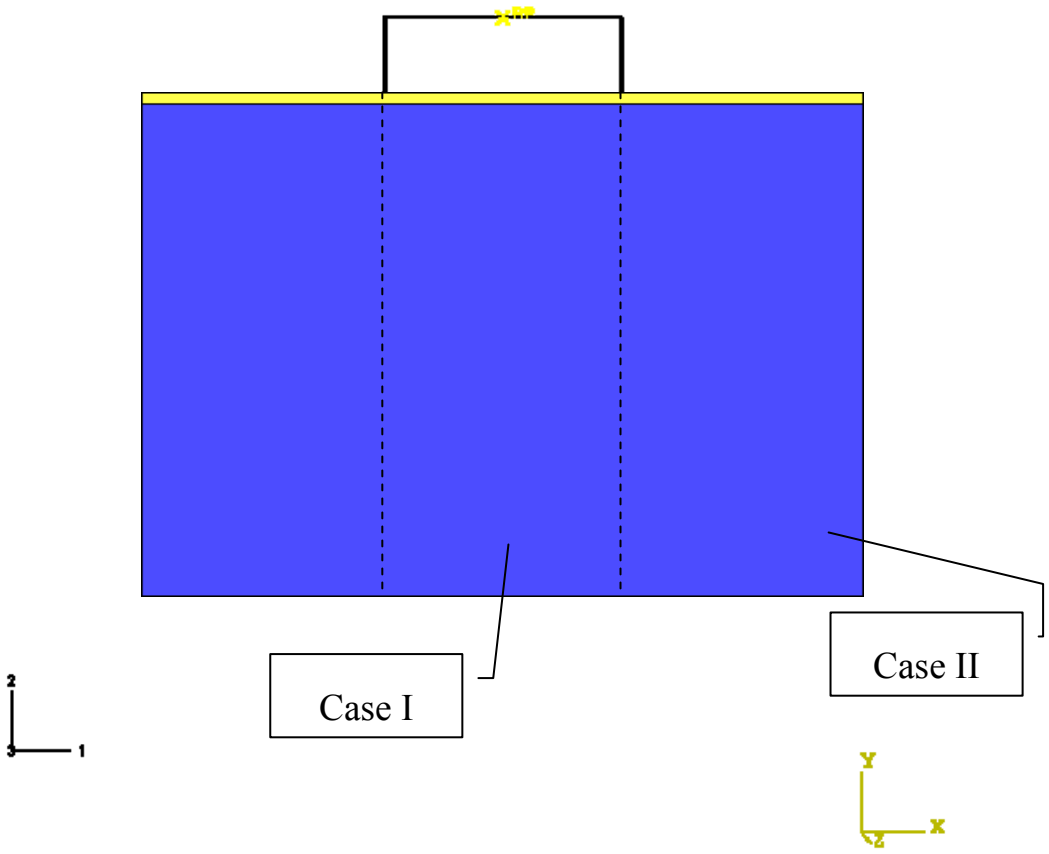

Fig 4-27 The geometry of the model for the continuous film case.

- The Geometry used in Fig 4-28 and Fig 4-29 are summarized as follow:

  The width of the indenter 5 μm and the width of the film are 5 μm (case I) 30 μm (case II).

  The thickness of film: 0.5 μm

  The thickness of substrate: 20.5 μm

  The thickness of interface: 0.001 μm

- The material properties of the film and substrate used for this simulation are summarized in Table 4-4 (these values are from indentation experiments)for soft film such as MSQ film[4]:

Table 4-4 Material properties for film and substrate.

	E [GPa]	**Poisson's ratio**	**Yield stress [GPa]**
Film	5.0	0.34	0.89
Substrate	112.4	0.28	3.1

The material properties for interface are set below:

In this case MAXS criterion is applied to simulate the fracture mechanism of interface and the three peak stress values for MAXS all equal to 0.5GPa, and the total fracture energy is set to be the value of 5N/m, and the interface stiffness if set to be 5000 GPa.

4.7.3 Discussion:

Fig. 4-28 and Fig. 4-29 are the load- penetration curves for thin film/substrate systems with the thickness of $5\,\mu m$ and $30\,\mu m$ respectively. The critical penetration depths of the indenter in these two figures are almost the same. However, the critical load for thin film with $30\,\mu m$ width is much bigger than that of the value for the thin film with $5\,\mu m$ width, because the only difference in the two cases is the width, therefore, the significant different critical loads most likely due to the length of the film. This simple simulation suggested that a full 3-dimensional model is needed in order to comparing the experimental and simulation results properly.

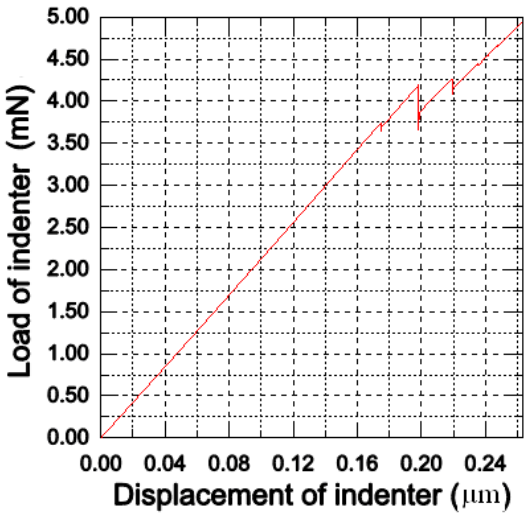

Fig 4-28 FEM simulated load-penetration curve for the case of the thin film with 5 μm width

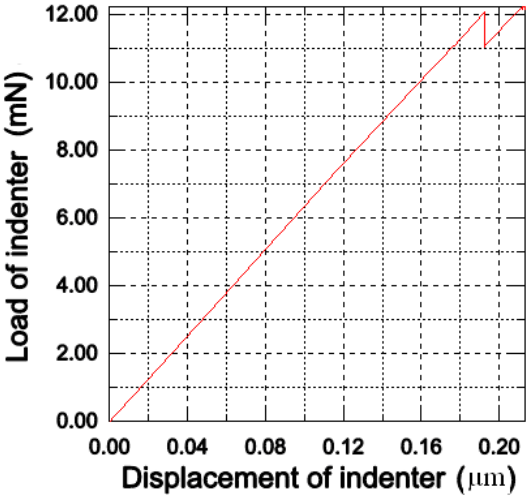

Fig 4-29 FEM simulated load-penetration curve for the case of the thin film with 30 μm width

REFERENCES:

[1] H. Jiang, Master thesis, Department of Materials Science, NUS, 2005.

[2] Y.W. Zhang , K.Y. Zeng, and R. Thampurun, Materials Science and Engineering, A319–321 (2001) 893.

[3] P. Liu, Y.W. Zhang, K.Y. Zeng , C. Lu, and K.Y. Lam, Engineering Fracture Mechanics, 74 (2007) 1118.

[4] K. B. Yeap. K. Y. Zeng, H. Y. Jiang, L. Shen and D.Z. Chi, J. Appl. Phys, 101, (2007), 123531.

Chapter 5 Experiments and Discussion

5.1 Methodology

In this chapter we will compare the result of simulation with that of the nano-indentation experiments. The angle of indenter tip is 90° for both cases. For nanoindentation experiments, the film is BD (black diamond) film and the thickness of films varies from 100 nm to 1000 nm. The elastic modulus and hardness of the films were measured by standard nanoindentation method and the results are summarized in Table 5-1.

Table 5-1 The material properties for the three films

Modulus[GPa]	***BD 100nm***	***BD 300nm***	***BD 500nm***	***BD 1000nm***
AVE	14.44	11.69	9.15	9.7
STD	5.35	5.63	1.08	0.39
Hardness[GPa]	***BD 100nm***	***BD 300nm***	***BD 500nm***	***BD 1000nm***
AVE	1.88	1.66	1.67	1.69
STD	0.76	0.23	0.11	0.19
Yield stress[GPa]	0.95	0.88	1.03	1.01

5.2 Compare Simulation with Experiment

As discussed in the section 4.7, due to the effect of the wedge length, the critical load from simulation may be smaller than that from experiment. Fig 5-1 and Fig 5-2 show the simulated and experimental wedge indentation load-penetration curves for thin film with the thickness of 100 nm,

respectively. Fig 5-3 and Fig 5-4 are the same curves for 300 nm thickness film. Fig 5-5 and Fig 5-6 are the curves for 500 nm film. During the simulation, the mechanical properties of the film were set the same for all the thickness, where as the properties of substrate were set same as these of Si, the interface properties were also set same as before. Because the simulation only analysis half of the thin film/substrate system when considering the symmetry of the system geometry and the total load of indenter should include another half, therefore the load from wedge indentation simulation is only half of the value in real case. Compared these curves with the result from experiments (Fig 5-2, Fig 5-4, Fig 5-6), it can be seen that the total load calculated from simulation is in general smaller than these from experiments, same as what discussed in the section 4.7. Another difference between the experiments and the simulation is that the experiments are done under load control, since all of the commercial nanoindenters are designed with load-control mode, and the simulation is under displacement control, therefore, when interface delamination occurs, the simulation will show a load-drop but the experiments will show a displacement pop-up under the constant load.

According to Fig 5-1, for the case of 100 nm thickness film, there is no significant load drop in the simulated load-displacement curve, similarly, there is no clear pop-up can be seen in the experimental load-displacement curve (Fig 5-2). This phenomenon is possibly due to the fact of the thickness of film is too thin to have a significant influence in the load-penetration curve when

crack happens.

However, despite the differences in the critical indentation loads, the value of critical penetration depths for the load-drop in the simulated indentation load-displacement curve and the displacement pop-ups in the experimental load-displacement curve are agreed reasonable well if comparing Fig 5-3 to Fig. 5-4, and Fig. 5-5 to Fig 5-6 for the films with different film thicknesses. This is the same as reported by Yeap et al [1]. As have mentioned earlier, more precise comparison needs to have a full 3-D simulation model.

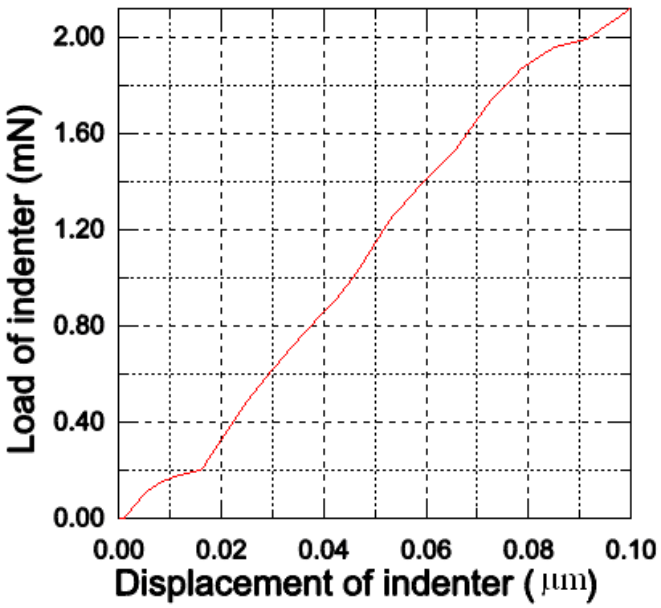

Fig 5-1 FEM simulated load—penetration curve for thin film with thickness of 100 nm

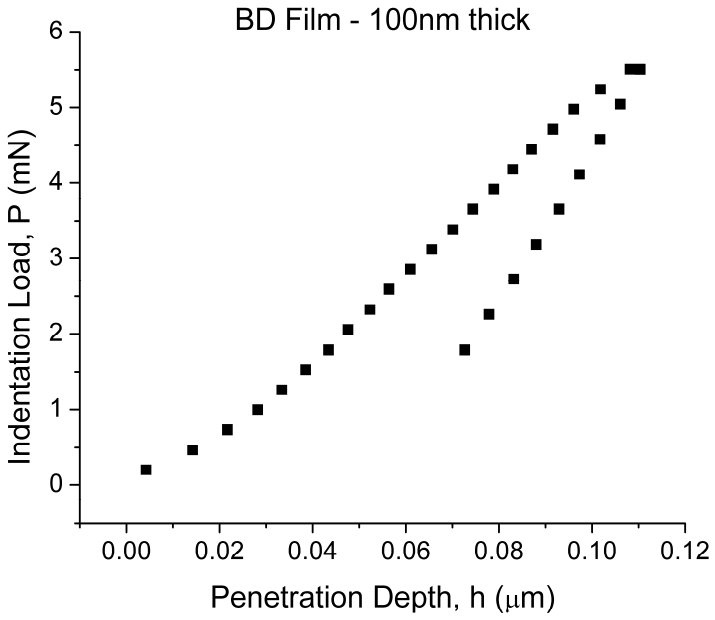

Fig 5-2 Experimental load—penetration curve for thin film with thickness of 100 nm

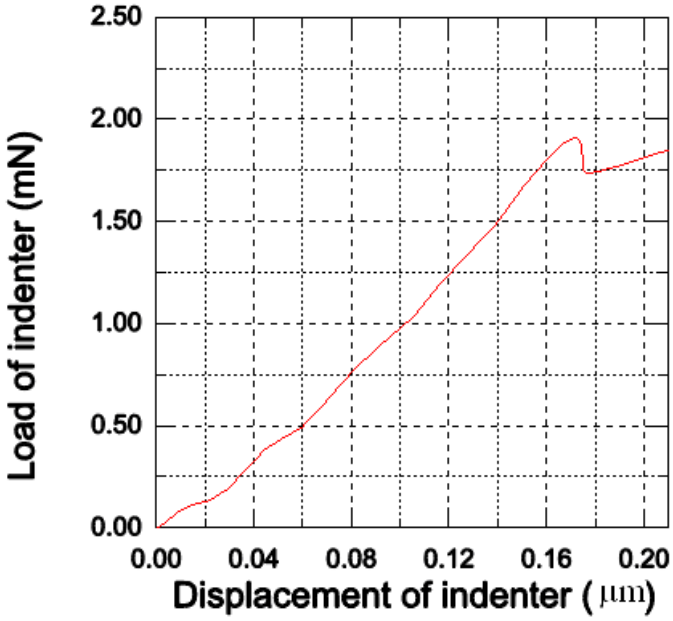

Fig 5-3 FEM simulated load—penetration curve for thin film with thickness of 300 nm

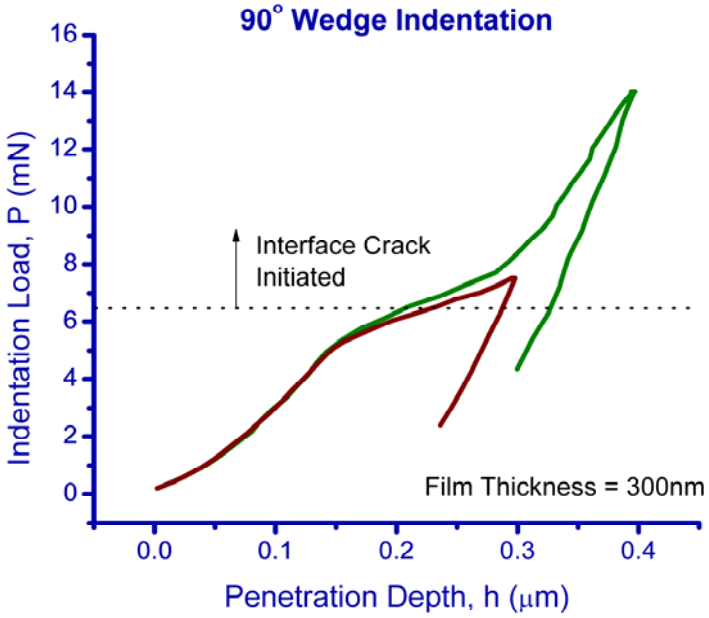

Fig 5-4 Experimental load—penetration curve for thin film with thickness of 300 nm

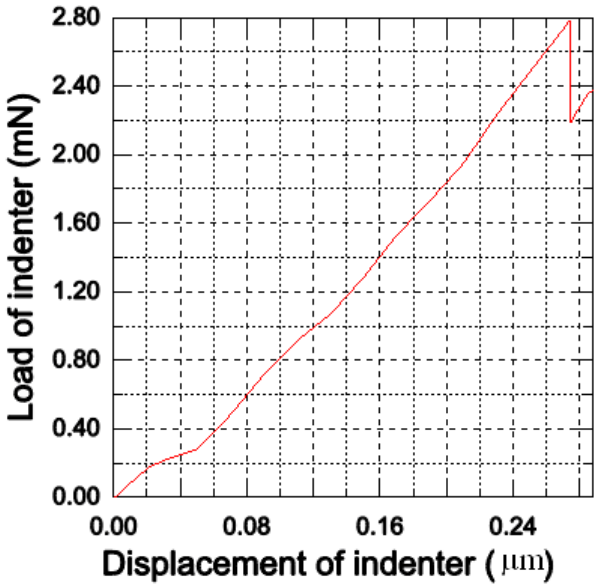

Fig 5-5 FEM simulated load—penetration curve for thin film with thickness of 500 nm

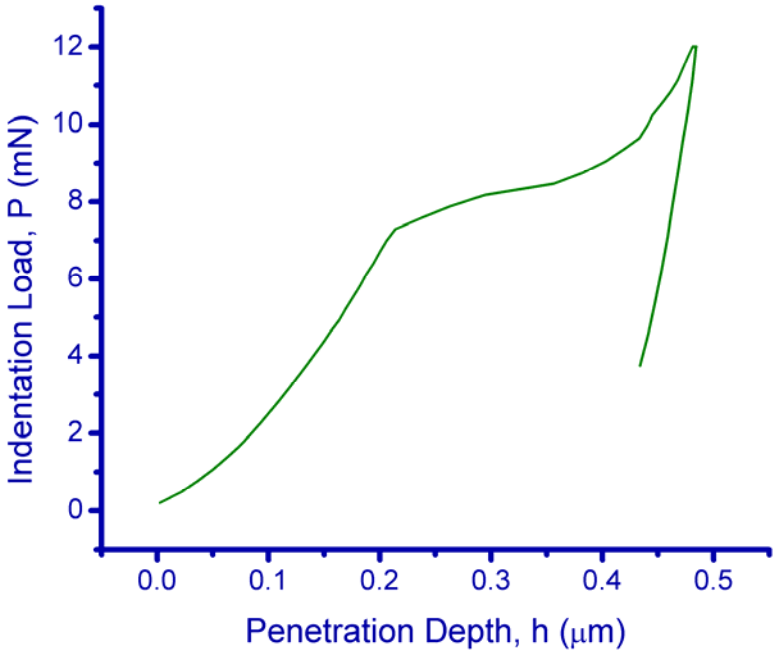

Fig 5-6 Experimental load—penetration curve for thin film with thickness of 500 nm

5.3 The Results for Different Indenter Tip Angles

During nano-indentation experiments, the angle of indenter tip is another factor which will affect the interfacial delamination properties. Fig 5-7 to Fig 5-9 show the load-penetration curves for indentations with 120° indenter tip. If compared with the results from the Section 5.2, Fig 5-1, Fig 5-3 and Fig 5-5, it can be seen that, for the same thin/film substrate systems, different indenter tip angle will cause some difference on the critical load and critical depth for delamincation. For instance, for the indentation of 500 nm thickness film with 90° indenter tip (Fig.5-5), the critical indentation load is about 2.75 mN and the critical indentation depth is more than 0.25 μm, however for indentation with 120° indenter tip on the same film (Fig.5-9), the critical load is 2.8 mN and the critical depth is about 0.2 μm. Similar cases can be seen from the simulation of the wedge indentation of the films with other thickness. The result shows that the critical indentation load for 120^{o} indenter is higher than that of the 90^{o} indenter, while the critical indentation depth is lower. This can be understood that as the angle of indenter tip increase, the contact area between indenter and the film become larger, so that it will need higher load to reaches to the same indentation depth. Hence the critical indentation load is higher, however, the critical indentation depth is lower for the interfacial delamination, this may be due to the higher indentation load induce the interfacial delamination earlier. In addition, with the angle increase, the indenter may have more influence on the interface in shear direction

(direction-2), and according to the discussion in the section 4.5 the crack will initiate in mode II, therefore if the angle of the indenter tip increase, it will make the interface crack initiate before the indenter reach the critical depth for 90^{o} indenter case.

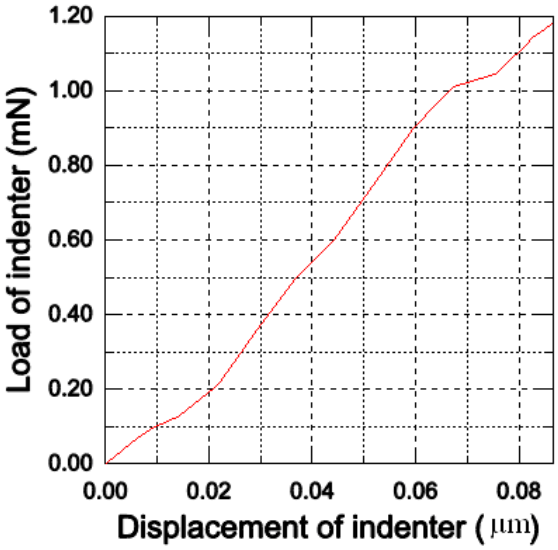

Fig 5-7 FEM simulated load—penetration curve for thin film with thickness of 100 nm (indenter tip angle is 120°)

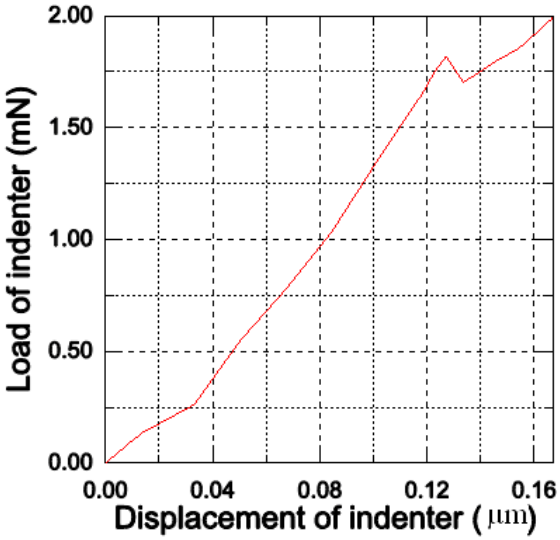

Fig 5-8 FEM simulated load—penetration curve for thin film with thickness of 300 nm (indenter tip angle is 120°)

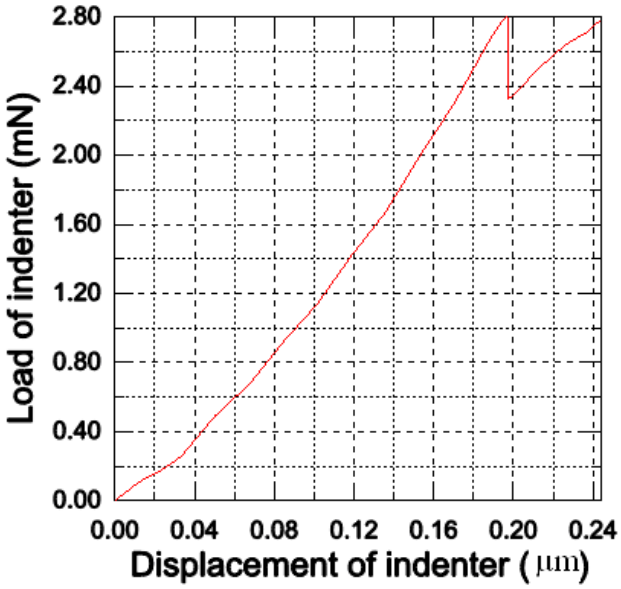

Fig 5-9 FEM simulated load—penetration curve for thin film with thickness of 500 nm (indenter tip angle is 120°)

REFERENCES:

[1] K.B. Yeap, K.Y. Zeng, H.Y. Jiang. L. Shen and D.Z.Chi, J.

Apply Phys.,101, 123531,(2007)

Chapter 6 Conclusions and Future Work

6.1 Conclusions

The thin film/substrate structure contains three sections: film, substrate and the interface between the film and substrate. In this thesis, the fracture behavior of interfaces during wedge indentation experiments has been investigated by using finite element simulations with cohesive zone models. This thesis investigates effects of the three important factors in cohesive zone models; interface strength, interface energy and the shape of traction separation law on the indentation characteristics and the interface delamination processes. Other than that, the shape of indenters and the thickness of film may also affect the fracture behavior of the interface in thin film/substrate systems. In addition, this thesis also investigated how to incorperate the cohesive zone model in the FEM simulation in ABAQUS and apply the methodology to the case of wedge indentation. It is hope that this thesis can provide some groundwork for future simulation studies in this area.

The simulation results show that there would be a significant drop of the load in the indentation P-h curve, which indicates the crack initiates at the interface. This conclusion also suggests that the indentation P-h curve could be a useful tool to determine the fracture behaviors of the interface. In addition, according to the indentation P-h curves and numerical results from simulation,

the interface crack is found to initiate as mode II fracture.

This thesis also investigated the influence of film thickness and film properties on the critical indentation load and critical indentation depth, which are the load and penetration depth of indenter when a crack initiates at the interface of thin film/substrate systems during wedge indentation experiments. The result shows that for a film with pure elastic properties, both the critical load and critical depth will increase linearly with the film thickness, but for a film with elastic-perfectly-plastic properties, the critical load and critical depth will show non-linear behavior. The critical indentation loads for the films with elastic-perfectly-plastic property is significantly lower than that for the film with purely elastic properties, however, the critical indentation depths are similar in both cases.

The effects of indenter angles on the interface delamination are also studied. Increasing the indenter angles will increase the critical indentation load for delamination, however, the critical indentation depth will decrease for a large angle of indenters.

A simple model is built to study the effects of wedge length on the interface delamination behavior. It is found that with increasing length of the wedge tip, the critical indentation load increased significantly. This finding will help to make proper comparison between the simulation and experimental results in the future.

6.2 Future Work

To further investigate the fracture mechanisms of an interface in thin film/substrate systems, a full three dimensional model may be built because of the wedge length effect discussed in the Chapters 4 section 7. To determine the material properties of an interface in three dimensional cohesive zone models, it is necessary to combine the simulation method with nanoindentation experiments.

The behaviors of film and substrate in this thesis are assumed to be elastic perfectly plastic, future simulation should consider the strain hardening of film and substrate.

Furthermore, the effects of wedge angles on the interface delamination processes need to be studied in more details. As we have seen from the simulation, three parameters are needed for the FEM simulation with ABAQUS using cohesive zone model: interfacial strength, interfacial energy and interface stiffness, however, the experimental indentation load-displacement curve can only get one parameter, i.e., critical indentation load or critical indentation depth. Even with the assumed known interface stiffness, there would still need one more parameter from the indentation load-displacement curve, hence the indenter angle could be another key factor to use in order to derive more generalized methodology to characterize the interface properties from nanoindentation experiments.